Journal of Computational Physics 229 (2010) 6318–6342

Contents lists available at ScienceDirect

Journal of Computational Physics

journal homepage: www.elsevier.com/locate/jcp

High order quadratures for the evaluation of interfacial velocities in axi-symmetric Stokes flows

M. Nitsche [a,*], H.D. Ceniceros [b], A.L. Karniala [c], S. Naderi [a]

[a] Department of Mathematics and Statistics, University of New Mexico, Albuquerque, NM 87131, United States
[b] Department of Mathematics, University of California Santa Barbara, CA 93106, United States
[c] Birkerod Gymnasium and International Baccalaureate School, 3460 Birkerod, Denmark

ARTICLE INFO

Article history:
Received 2 January 2010
Received in revised form 25 April 2010
Accepted 27 April 2010
Available online 31 May 2010

Keywords:
Singular integrals
Boundary integral methods
Complete elliptic integrals
Axi-symmetric interfacial Stokes flow

ABSTRACT

We propose new high order accurate methods to compute the evolution of axi-symmetric interfacial Stokes flow. The velocity at a point on the interface is given by an integral over the surface. Quadrature rules to evaluate these integrals are developed using asymptotic expansions of the integrands, both locally about the point of evaluation, and about the poles, where the interface crosses the axis of symmetry. The local expansions yield methods that converge to the chosen order pointwise, for fixed evaluation point. The pole expansions yield corrections that remove maximal errors of low order, introduced by singular behaviour of the integrands as the evaluation point approaches the poles. An interesting example of roundoff error amplification due to cancellation is also addressed. The result is a uniformly accurate fifth order method. Second order, pointwise fifth order, and uniform fifth order methods are applied to compute three sample flows, each of which presents a different computational difficulty: an initially bar-belled drop that pinches in finite time, a drop in a strain flow that approaches a steady state, and a continuously extending drop. In each case, the fifth order methods significantly improve the ability to resolve the flow. The examples furthermore give insight into the effect of the corrections needed for uniformity. We determine conditions under which the pointwise method is sufficient to obtain resolved results, and others under which the corrections significantly improve the results.

1. Introduction

Boundary integral methods are an efficient choice to compute the motion of an interface separating two regions of fluid, such as the vortex sheet model for a shear layer, the boundary of drops and bubbles, the surface of water-waves, or of a solid object such as an airplane. The methods apply when the fluid on either side of the interface is modelled using linear equations, for example by potential flow, obtained in the inviscid limit of the Navier–Stokes equations, or by Stokes flow, obtained in the limit of zero inertial forces in which viscosity dominates. In both of these cases, the (nonlinear) interface velocity can be expressed as an integral along the interface, thus reducing the dimension of the problem. Under planar or axial symmetry, the problem reduces further to a one-dimensional one. This feature makes it possible to achieve, at least in principle, the high resolution necessary to investigate small scale phenomena, such as that occur during coalescence and breakup of bubbles or in the presence of surfactants.

* Corresponding author. Tel.: +1 505 277 4613; fax: +1 505 277 5505.
E-mail addresses: nitsche@math.unm.edu (M. Nitsche), hdc@math.ucsb.edu (H.D. Ceniceros), akarniala@gmail.com (A.L. Karniala), shadi@math.unm.edu (S. Naderi).

0021-9991/$ - see front matter © 2010 Elsevier Inc. All rights reserved.
doi:10.1016/j.jcp.2010.04.043

Boundary integral simulations of closed interfaces in Stokes flow include studies of the deformation and breakup of drops and bubbles in an external flow (see, e.g., [1,30,36,20,35,27,11,10,34,5,19,13]), coalescence [42,21,39], drop evolution in the presence of surfactants [14,33,15,4], and multiphase flow [6]. For axi-symmetric flow, the basic numerical approach was first described by Youngren and Acrivos [40]. Since then significant progress has been made in the extensions of the boundary integral formulation and on the development of more accurate and efficient methods, as reviewed by Pozrikidis [26,28]. Unfortunately, evaluating the axi-symmetric integrals is computationally expensive, and standard high order quadratures cannot be applied due to the integrands' intricate singular structure.

Our goal in this work is to analyze the line integrals in axi-symmetric Stokes flow, and develop higher order quadrature rules for them. The integrals describe the velocity at a point on the interface. To begin, we find asymptotic expansions of the integrands about the singularity at the point of evaluation. Guided by the work of Sidi and Israeli [32], these expansions yield systematically higher order modifications to the trapezoidal rule. Within this framework, we show that the popular "desingularized" trapezoidal rule [11] is second order accurate. The asymptotic analysis also shows that the leading order desingularization is only advantageous for the single layer potential but there is no apparent gain for the double layer potential.

We test the accuracy of the resulting quadratures on a simple example and find two issues that must be addressed. (1) The high order approximations are quickly overshadowed by the amplification of roundoff errors that occurs when highly singular terms in the double layer potential are subtracted from each other. We identify these terms and combine them in a suitable way to remedy the problem. (2) The modified trapezoid approximations converge pointwise at the specified rate, that is, for fixed evaluation point, but they do not converge uniformly. The maximal errors near the poles are of second order, and as a consequence the accuracy degrades around that region. This singular behaviour is an artifact of the axi-symmetric coordinate system and is similar to the one observed previously in axi-symmetric interfacial Eulerian flows [23,24]. Closely following this earlier work, we obtain asymptotic approximations to the present integrands near the poles and identify the low order terms in the error. These terms serve as corrections to the pointwise convergent method. They can essentially be precomputed and are added at minimal ($O(1)$) computational cost per timestep. The end result is a new, uniformly fifth order quadrature rule that adds little overhead to the commonly used second order approximations and thus can attain a given accuracy for a fraction of the computational cost. We note that in principle, the procedure described here can be used to obtain rules of arbitrarily uniformly high order.

We then apply the second order, the pointwise fifth order and the uniform fifth order methods to compute the evolution of three sample fluid flows, each of which presents a different computational difficulty. We show that in each case, the higher order methods significantly improve the ability to resolve the flow. The examples also illustrate the effect of the corrections required for uniformity of the high order methods. In certain cases, with resolutions used in practice, the low order error terms of the pointwise method are so small that the fifth order corrections do not impact the results. In other examples, the corrections significantly improve the results.

The paper is organized as follows. In Section 2, we briefly describe the boundary integral formulation for the motion of one drop in axi-symmetric Stokes flow and discuss the desingularization. In Section 3, we construct pointwise high order quadratures, address roundoff error amplification, and derive the pole corrections necessary for uniform fifth order accuracy. In Section 4, we apply the second order and fifth order rules to compute the evolution of three sample interfacial flows, and evaluate their relative performance. The results are summarized in Section 5. The appendices give all the necessary information to compute the corrections to fifth order and to determine their effect. The corrections can also be obtained directly from the corresponding author, after which the implementation is simple, consisting of a small change to the trapezoid rule.

2. Governing equations

2.1. The boundary integral formulation

We consider a drop of fluid with viscosity μ_d surrounded by a fluid of viscosity μ_e and affected by an external flow field $\mathbf{u}^\infty$. Neglecting inertia terms (Stokes flow) and assuming constant surface tension σ, the velocity $\mathbf{u}$ at a point $\mathbf{x}_0$ on the surface S of the drop can be written in the following boundary integral representation [31]

$$\mathbf{u}(\mathbf{x}_0) = \frac{2}{1+\lambda}\mathbf{u}^\infty(\mathbf{x}_0) - \frac{\sigma}{\mu_e(1+\lambda)}\mathbf{u}^s(\mathbf{x}_0) + \frac{1-\lambda}{1+\lambda}\mathbf{u}^d(\mathbf{x}_0), \tag{2.1}$$

where $\lambda = \mu_d/\mu_e$ and $\mathbf{u}^s$ and $\mathbf{u}^d$ are the single and double layer boundary integral contributions to the interfacial velocity, respectively. Their Cartesian components $u_j,\ j = 1,2,3$ are given by

$$u_j^s(\mathbf{x}_0) = \frac{1}{4\pi}\int_S G_{ij}(\mathbf{x}-\mathbf{x}_0)n_i(\mathbf{x})\kappa(\mathbf{x})dS(\mathbf{x}), \tag{2.2a}$$

$$u_j^d(\mathbf{x}_0) = \frac{1}{4\pi}PV\int_S T_{ijk}(\mathbf{x}-\mathbf{x}_0)n_k(\mathbf{x})u_i(\mathbf{x})dS(\mathbf{x}), \tag{2.2b}$$

where

$$G_{ij}(\mathbf{x}) = \frac{\delta_{ij}}{r} + \frac{x_i x_j}{r^3}, \tag{2.2c}$$

$$T_{ijk}(\mathbf{x}) = -6\frac{x_i x_j x_k}{r^5} \tag{2.2d}$$

are the free space Green's function (Stokeslet tensor) and the associated stress tensor, respectively, δ_{ij} is the Kronecker delta, $r = \|\mathbf{x}\|$, $\kappa = \nabla \cdot \mathbf{n}$ is the sum of the principal curvatures, and $\mathbf{n}$ is the outward unit normal. The summation convention over repeated indices is used, and the symbol *PV* in (2.2b) denotes the principal value of the singular integral.

For nonzero surface tension σ, (2.1) is nondimensionalized using the radius R of the initial bubble as the characteristic length scale, and $U = \sigma/\mu_e$ as the characteristic velocity. In addition, $\mathbf{u}^\infty$ is nondimensionalized by $U_\infty = GR$, where G is a characteristic strain rate of the external flow. That is, we introduce dimensionless velocities $\mathbf{u}' = \mathbf{u}/U$ and $\mathbf{u}^{\infty\prime} = \mathbf{u}^\infty/U_\infty$, and then drop the primes, to obtain the dimensionless equations

$$\mathbf{u}(\mathbf{x}_0) = \frac{2Ca}{1+\lambda}\mathbf{u}^\infty(\mathbf{x}_0) - \frac{1}{1+\lambda}\mathbf{u}^s(\mathbf{x}_0) + \frac{1-\lambda}{1+\lambda}\mathbf{u}^d(\mathbf{x}_0), \tag{2.3}$$

where $Ca = \mu_e GR/\sigma$ is a capillary number that measures viscous forces relative to surface tension forces. For zero surface tension σ, the single layer contribution vanishes and the nondimensional equations, obtained using R and any characteristic velocity U, are $\mathbf{u}(\mathbf{x}_0) = \frac{2}{1+\lambda}\mathbf{u}^\infty(\mathbf{x}_0) + \frac{1-\lambda}{1+\lambda}\mathbf{u}^d(\mathbf{x}_0)$. In all our examples hereon we consider $\sigma > 0$, that is, (2.3).

This paper concerns axi-symmetric flows with no swirl. In this case, the integration with respect to the angular variable ϕ (see Fig. 1(a)) can be performed analytically to reduce the boundary integrals (2.2) to line integrals over a curve C. This curve, shown in Fig. 1(b), is the cross-section of S with the x–y plane, where y is the axial coordinate and $x \geqslant 0$ is the radial coordinate. The curve at time t is parametrized by

$$C: \quad (x(\alpha,t), y(\alpha,t)), \quad 0 \leqslant \alpha \leqslant \pi.$$

Throughout this work, we assume the surface intersects the axis of symmetry, with the endpoints $\alpha = 0, \pi$ corresponding to the poles, that is, the points were $r = 0$.

The velocity at a point $\alpha = \alpha_j$ on C is $\mathbf{u}(\alpha_j, t) = (u(\alpha_j, t), v(\alpha_j, t))$ where u, v are the radial and axial components, respectively. Their single and double layer components (2.2) reduce to the line integrals

$$u^s(\alpha_j,t) = -\frac{1}{4\pi}\int_0^\pi H^{us}(\alpha,\alpha_j,t)\kappa(\alpha,t)d\alpha, \tag{2.4a}$$

$$v^s(\alpha_j,t) = -\frac{1}{4\pi}\int_0^\pi H^{vs}(\alpha,\alpha_j,t)\kappa(\alpha,t)d\alpha, \tag{2.4b}$$

$$u^d(\alpha_j,t) = \frac{1}{4\pi}\int_0^\pi H_1^{ud}(\alpha,\alpha_j,t)u(\alpha,t) + H_2^{ud}(\alpha,\alpha_j,t)v(\alpha,t)d\alpha, \tag{2.4c}$$

$$v^d(\alpha_j,t) = \frac{1}{4\pi}\int_0^\pi H_1^{vd}(\alpha,\alpha_j,t)u(\alpha,t) + H_2^{vd}(\alpha,\alpha_j,t)v(\alpha,t)d\alpha, \tag{2.4d}$$

where

$$H^s(\alpha,\alpha_j,t) = M_1(x,x_j,y-y_j)\dot{y}(\alpha,t) - M_2(x,x_j,y-y_j)\dot{x}(\alpha,t), \tag{2.5a}$$

$$H_l^d(\alpha,\alpha_j,t) = Q_{l1}(x,x_j,y-y_j)\dot{y}(\alpha,t) - Q_{l2}(x,x_j,y-y_j)\dot{x}(\alpha,t), \tag{2.5b}$$

and $l = 1, 2$. Here $x = x(\alpha,t)$, $y = y(\alpha,t)$, $x_j = x(\alpha_j,t)$, $y_j = y(\alpha_j,t)$ and the dot stands for differentiation with respect to α. The absence of superscript u, v in (2.5ab) and throughout the rest of this paper implies that the equation holds for both the u and

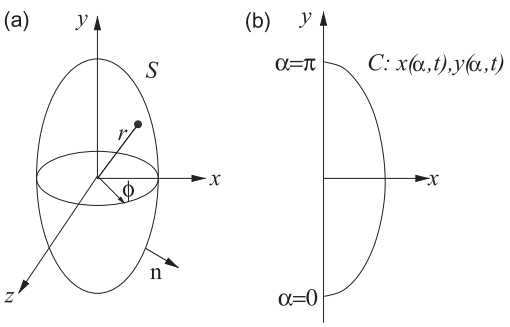

Fig. 1. Sketch showing (a) axi-symmetric surface S with outward normal $\mathbf{n}$, symmetry-axis y, and azimuthal angle Φ, (b) cross-section C in the x–y plane, with poles labeled by $\alpha = 0, \pi$.

the v components. The functions M and Q depend in an intricate way on the complete elliptic integrals of the first and second kind and are provided in Pozrikidis [26, Section 2.4]. We list them in Appendix A in a form that we find more convenient to our purposes. The curvature κ is

$$\kappa = \frac{\dot{y}}{x\sqrt{\dot{x}^2+\dot{y}^2}} + \frac{\dot{x}\ddot{y}-\dot{y}\ddot{x}}{(\dot{x}^2+\dot{y}^2)^{3/2}}. \tag{2.6}$$

Note that the integrals in (2.4cd) are no longer singular and do not require evaluation in the principal value sense. Summary derivations of these results can be found in Pozrikidis [26] and Zapryanov and Tabakova [41].

2.2. The integrands

Each of the integrands in (2.4) is a function of α, α_j, and t which we denote generically by $G(\alpha,\alpha_j,t)$. For $\alpha_j \neq 0,\pi$, these functions have integrable logarithmic singularities at $\alpha=\alpha_j$. Using expansions of the complete elliptic integrals about $\alpha=\alpha_j$ and Mathematica, we find that

$$G(\alpha,\alpha_j,t) = \widetilde{G}(\alpha,\alpha_j,t) + \sum_{k=0}^{\infty} c_k(\alpha_j,t)(\alpha-\alpha_j)^k \log|\alpha-\alpha_j|, \tag{2.7}$$

where $\widetilde{G}$ is smooth. For the single layer, $c_0 \neq 0$ and thus the integrand is unbounded (but integrable) at $\alpha=\alpha_j$. The double layer is more regular with $c_0=0$. The asymptotic form (2.7) of the integrands and the modified Euler–Maclaurin formula of Sidi and Israeli [32] are the central building principle for the high order quadrature rules we propose in this work.

For $\alpha_j = 0,\pi$, the integrands are smooth, with $c_k = 0$ for all k. For completeness, the integrands obtained by taking the limit of $G(\alpha,\alpha_j,t)$ as $\alpha_j \to 0,\pi$ are listed in Appendix B.

2.3. Leading order desingularization

An approach commonly taken in previous numerical studies is the following. For the single layer, the identity $\int_0^\pi H^s(\alpha,\alpha_j,t)d\alpha = 0$, which follows from incompressibility [26], is used to rewrite

$$u^s(\alpha_j,t) = -\frac{1}{4\pi}\int_0^\pi H^{us}(\alpha,\alpha_j,t)[\kappa(\alpha,t)-\kappa(\alpha_j,t)]d\alpha, \tag{2.8a}$$

$$v^s(\alpha_j,t) = -\frac{1}{4\pi}\int_0^\pi H^{vs}(\alpha,\alpha_j,t)[\kappa(\alpha,t)-\kappa(\alpha_j,t)]d\alpha. \tag{2.8b}$$

This removes the leading order singular term of the integrands in (2.4ab). That is, the integrands in (2.8ab) are of the asymptotic form (2.7) with $c_0=0$ instead of $\neq 0$. The higher order logarithmic terms remain.

In previous work, this desingularization has the effect of increasing the order of convergence of the methods used from $O(h\log h)$ to second order, *uniformly over the whole interface*. This will follow from our analysis below. For the quadrature rules we propose here, using (2.8ab) simplifies the implementation mainly because the new integrands have less singular behaviour at the poles. This will be described in Section 3.3.

A similar procedure is also commonly used for the double layer components. It is possible to use another flow identity to rewrite

$$u^d(\alpha_j,t) = \frac{1}{4\pi}\int_0^\pi [H_1^d(\alpha,\alpha_j,t)u(\alpha,t) - H_1^{d'}(\alpha,\alpha_j,t)u(\alpha_j,t)] + [H_2^d(\alpha,\alpha_j,t)v(\alpha,t) - H_2^{d'}(\alpha,\alpha_j,t)v(\alpha_j,t)]d\alpha, \tag{2.9}$$

and similarly for v^d. The formulas for H' are given by Davis [11]. However, due to the orientational dependence of the integrand, $H \neq H'$. Using Mathematica, we find that the new integrands (2.9) are no less singular than the original ones (2.4cd). Both are bounded, of the form (2.7) with $c_0=0$. As a result, no gain is achieved using this formulation. Thus, in this work we extract the leading order singular term in the single layer only, but not in the double layer. The resulting integrands in each case, denoted by G throughout the rest of this paper, are given by

$$G_s(\alpha,\alpha_j,t) = H_s(\alpha,\alpha_j,t)[\kappa(\alpha,t)-\kappa(\alpha_j,t)], \tag{2.10a}$$

$$G_d(\alpha,\alpha_j,t) = H_d^1(\alpha,\alpha_j,t)u(\alpha,t) + H_d^2(\alpha,\alpha_j,t)v(\alpha,t), \tag{2.10b}$$

where both G_s and G_d are of the form (2.7) with $c_0=0$.

3. Quadrature rules

3.1. Pointwise approximations

Sidi and Israeli [32] showed that for any function of the form (2.7),

$$\int_a^b G(\alpha,\alpha_j,t)d\alpha = h\sum_{\substack{k=0\\k\neq j}}^{N}{}'' G(\alpha_k,\alpha_j,t) + h\widetilde{G}(\alpha_j,\alpha_j,t) + c_0(\alpha_j,t)h\log\frac{h}{2\pi} + \sum_{\substack{k=2\\k\ \text{even}}}^{m} v_k c_k(\alpha_j,t)h^{k+1} + \sum_{\substack{k=1\\k\ \text{odd}}}^{m}\gamma_k\left[\frac{\partial^k G}{\partial\alpha^k}(b,\alpha_j,t) - \frac{\partial^k G}{\partial\alpha^k}(a,\alpha_j,t)\right]h^{k+1} + O(h^{m+2}) \tag{3.1}$$

for any integer $m \geqslant 0$. Here $\alpha_k = a + kh,\ k = 0,\ldots,N$, is a uniform partition of $[a,b]$ of meshsize $h = (b-a)/N$. The double prime on the summation indicates that the first and last summands are weighted by 1/2. The constants appearing in (3.1) relevant to our discussion below are $\gamma_1 = -1/12,\ \gamma_3 = 1/720$, and $v_2 = -0.06089691411678654156\ldots$

Eq. (3.1) is a modified Euler–Maclaurin formula with which one can approximate the integrals to arbitrarily high order. By truncating the sum on the right hand side at any desired point, one obtains a quadrature rule of known order, $T[G]^h_{[a,b]}$, and moreover, with a known expansion for the approximation error, which we denote throughout by

$$E[G]^h_{[a,b]} = \int_a^b G(\alpha,\alpha_j,t)d\alpha - T[G]^h_{[a,b]}. \tag{3.2}$$

However, note that since all terms in the sum (3.1), in particular all c_k and $\partial^k G/\partial\alpha^k$, depend on α_j (and t), so does the error, and the order of convergence therefore applies only pointwise, for fixed α_j. We will see below that the maximum error over all j does not necessarily decrease with the same order.

We remark that Sidi and Israeli [32] also considered more general principal value integrals of functions with singularities such as $1/(\alpha-\alpha_j)$, but those are not relevant to our present discussion.

3.1.1. Pointwise second order approximation

As an example, consider the approximation

$$T_2[G]^h_{[0,\pi]} = h\sum_{\substack{k=0\\k\neq j}}^{N}{}'' G(\alpha_k,\alpha_j,t) + h\widetilde{G}(\alpha_j,\alpha_j,t) \tag{3.3}$$

to compute the single and double layer velocities. Since after desingularizing the single layer, $c_0(\alpha_j,t) = 0$, it follows from (3.1) that the pointwise approximation error is $O(h^2)$. This simple trapezoidal rule has been employed for many years in boundary integral computations of Stokes flows [11,28], where $\widetilde{G}(\alpha_j,\alpha_j,t)$ is commonly evaluated by interpolation.

We remark that without the single layer desingularization, the trapezoidal rule (3.3) would be $O(h\log h)$. However the impact the desingularization has on the coefficients $c_k,\ \partial^k G/\partial^k\alpha$ in the error is more significant. As will follow from our results in Section 3.3, the desingularization sufficiently smooths the behaviour of the coefficients so that all terms in the error are uniformly bounded in α_j,

$$\max_{0\leqslant j\leqslant N} E_2[G]^h_{[0,\pi]}(\alpha_j,t) \leqslant c(t)h^2. \tag{3.4}$$

This would not be the case if, instead of desingularizing, one would find $c_0 \neq 0$ and use the first three terms in (3.1) to approximate the more singular integral. The commonly used trapezoidal rule (3.3) therefore requires the single layer desingularization to yield uniformly second order results.

3.1.2. Pointwise fifth order approximation

We are interested in a higher order approximation and consider here the fifth order rule:

$$T_5[G]^h_{[0,\pi]} = h\sum_{\substack{k=0\\k\neq j}}^{N}{}'' G(\alpha_k,\alpha_j,t) + h\widetilde{G}(\alpha_j,\alpha_j,t) + c_0(\alpha_j,t)h\log\frac{h}{2\pi} + v_2 c_2(\alpha_j,t)h^3 + \sum_{\substack{k=1\\k\ \text{odd}}}^{3}\gamma_k\left[\frac{\partial^k G}{\partial\alpha^k}(\pi,\alpha_j,t) - \frac{\partial^k G}{\partial\alpha^k}(0,\alpha_j,t)\right]h^{k+1} \tag{3.5}$$

with corresponding error

$$E_5[G]^h_{[a,b]} = \sum_{\substack{k=4\\k\ \text{even}}}^{m} v_k c_k(\alpha_j,t)h^{k+1} + \sum_{\substack{k=5\\k\ \text{odd}}}^{m}\gamma_k\left[\frac{\partial^k G}{\partial\alpha^k}(\pi,\alpha_j,t) - \frac{\partial^k G}{\partial\alpha^k}(0,\alpha_j,t)\right]h^{k+1} + O(h^{m+1}) \tag{3.6}$$

for any integer $m \geqslant 4$. To implement quadrature (3.5), one needs the coefficients c_2 of the integrands G, the values $\widetilde{G}(\alpha_j,\alpha_j,0)$, and their first and third derivatives at the endpoints. The corresponding values for G_s^{uv} and G_d^{uv} are given in Appendix C. Here, all the required derivatives of $x,\ y$ and κ are evaluated spectrally.

As a test, we apply (3.5) to compute the single and double layer components of the velocity of a sample interface at a fixed time $t = 0$, given by

$$x(\alpha, 0) = \sin(\alpha), \tag{3.7a}$$

$$y(\alpha, 0) = -\cos(\alpha) + \epsilon \cos^2(\alpha) \tag{3.7b}$$

with $\epsilon = 0.15$, and no external flow, $Ca = 0$.

Note that unless $\lambda = 1$, the double layer contribution turns (2.4cd) into a coupled system of Fredholm integral equations of the second type for the velocity components. As $\lambda \to 0$, the corresponding eigenvalues tend to 0 and the system becomes singular. This problem can be addressed using Wielandt's deflation algorithm (see, e.g., [11]). In the applications in Section 4, we use $\lambda > 0$ and solve the discrete linear system using GMRES. However, throughout Section 3, in order to more clearly separate the contributions to the error arising from the integration of G^s and from that of G^d, we integrate G^d using a specified (u, v) in the right hand side of (2.4cd). Specifically, we set $u(\alpha) = \sin\alpha$, $v(\alpha) = \cos\alpha$ in the integrand, chosen so that they satisfy the correct symmetries about the axis, and we report on the errors in integrating $G_s,\ G_d$ for these predetermined u and v.

We apply quadrature (3.5) with $h = \pi/N$, N = 32, 64, 128, 256, 512, 1024, 2048, and approximate the integration error by

$$E_5[G]^h_{[0,\pi]} \approx T_5[G]^{\pi/2048}_{[0,\pi]} - T_5[G]^h_{[0,\pi]}. \tag{3.8}$$

The error is shown in Fig. 2, as a function of α_j. Figures (a) and (b) show the errors for $G^{us},\ G^{vs}$. Figures (c) and (d) show the errors for $G^{ud},\ G^{vd}$ where the functions $u,\ v$ in the integrand are replaced by known functions, as described above.

As expected, for any fixed value of α_j the errors decrease as h^5 until roundoff error dominates the results. However, two unexpected observations can be made.

1. *Roundoff error*: Even though the computations are made in double machine precision, the double layer velocities exhibit unacceptably large roundoff errors of order 10^{-7} in Fig. 2(c) and somewhat smaller, of order 10^{-10}, in Fig. 2(d). We note that these large errors are not caused by an inaccurate evaluation of the complete elliptic integrals $F(k)$ and $E(k)$, as $k \to 0$. These integrals are computed accurately and quickly using the algorithm of Bulirsch [8]. (An alternative is to compute

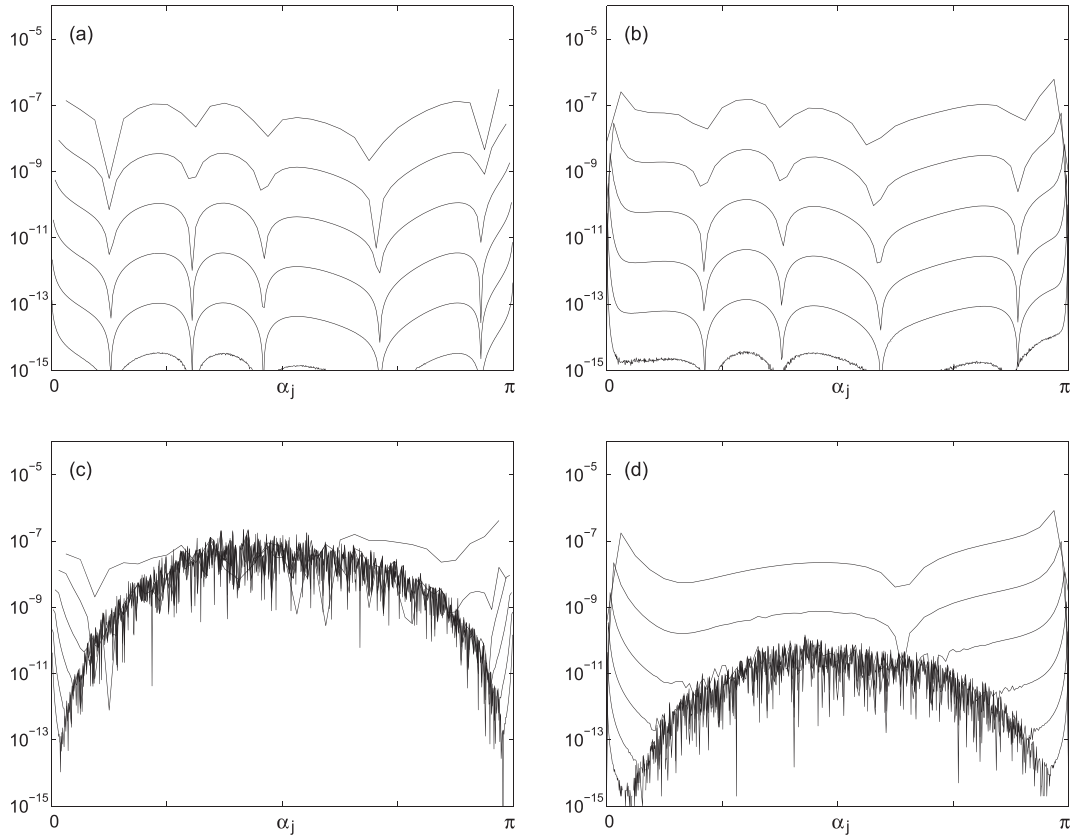

Fig. 2. Approximation error $E_5[G]^h_{[0,\pi]}$ vs. α_j, using $h = \pi/N$, N = 32, 64, 128, 256, 512, 1024, for G equal to (a) G^{us}, (b) G^{vs}, (c) G^{ud}, (d) G^{vd}, as given in (2.10) with $u(\alpha) = \sin\alpha$, $v(\alpha) = \cos\alpha$.

them using expansions for $F(k)$ and $E(k)$ to desired order, as in Lee and Leal [18].) As we will see, the large roundoff errors are instead the result of delicate linear combinations of highly singular terms.

2. *Loss of accuracy near the poles* $\alpha_j = 0, \pi$: Even though the error decays pointwise as $O(h^5)$, the error shown in Fig. 2 deteriorates near the poles, $\alpha_j = 0, \pi$. The maximum error appears to occur almost at the poles (after disregarding roundoff errors), and seems to decay more slowly than the error away from the poles. Indeed, the maximum error occurs at $j = 1$ and $j = N - 1$. That is, it does not occur at a fixed value of α_j, but at $\alpha_j = h$ and $\pi - h$. To find its decay rate, Fig. 3 plots the maximum errors near the poles as a function of h (+) and a line (−) with the indicated slope. The data is well approximated by the lines, showing that instead of $O(h^5)$, the maximum errors are fourth order for G^{us}, third order for G^{vs} and G^{vd}, and second order for G^{ud}. Thus the fifth order approximation T_5 (3.5) is not uniformly of fifth order, but apparently of second order only. This should be disturbing and put in question the high order accuracy of the solution after long-time computations of the interface evolution.

In the remainder of Section 3, we explain the origin of these two problems and how to overcome them, and present a uniformly fifth order accurate quadrature. In Section 4, we investigate the effect of these errors on long-time computations of interface evolution.

3.2. Removing roundoff error

To find the source of the roundoff error amplification apparent in Fig. 2(c) and (d), we have to look closely at the intricate, singular structure of G^{ud} and G^{vd}. We refer to the functions listed in Appendix A for this purpose.

G^{ud} and G^{vd} are functions of Q_{ik}'s. The functions Q_{ik} in turn are a sum of terms proportional to the integrals I_{5j}. For example,

$$Q^u_{11} = -6x[x^3 I_{51} - x^2 x_j (I_{50} + 2I_{52}) + x x_j^2 (I_{53} + 2I_{51}) - x_j^3 I_{52}]. \tag{3.9}$$

The Q's and the I's are singular at $\alpha = \alpha_j$, equivalently, at $(x, y) = (x_j, y_j)$ or $k = 1$, where k is as defined in Eq. (A.3). As noted in Appendix A, (A.6), the I's appearing in the right hand side of (3.9) behave as

$$I_{5j} \sim F_{sing} = \frac{8}{3c^5(1-k^2)^2} \sim \frac{1}{(\alpha - \alpha_j)^4} \quad \text{as } k \to 1, \text{ or equivalently, } \alpha \to \alpha_j. \tag{3.10}$$

However, the Q's appearing in the left hand side of sample equation (3.9) are less singular. Using Mathematica, we find that

$$Q_{ik} \sim \frac{1}{\alpha - \alpha_j} \quad \text{as } \alpha \to \alpha_j. \tag{3.11}$$

This shows that analytically the large singular components in I_{5j} cancel by subtraction. Performing this operation in finite machine precision leads to large loss of digits of accuracy and a consequently large roundoff error. (We remark that even though the Q_{ik} all are singular as in (3.11), the combination $Q_{l1}\dot{y} - Q_{l2}\dot{x}$ given in (2.5b) that defines the Stokes flow integrands is less singular, as in (2.7).)

To remedy the roundoff error amplification problem, we extract the singular component from I and compute

$$I'_{ij} = I_{ij} - F_{sing}. \tag{3.12}$$

This is done by first removing the singular component from $E_{5/2}$:

$$E'_{5/2} = E_{5/2} - \frac{2}{3(1-k^2)^2} \tag{3.13}$$

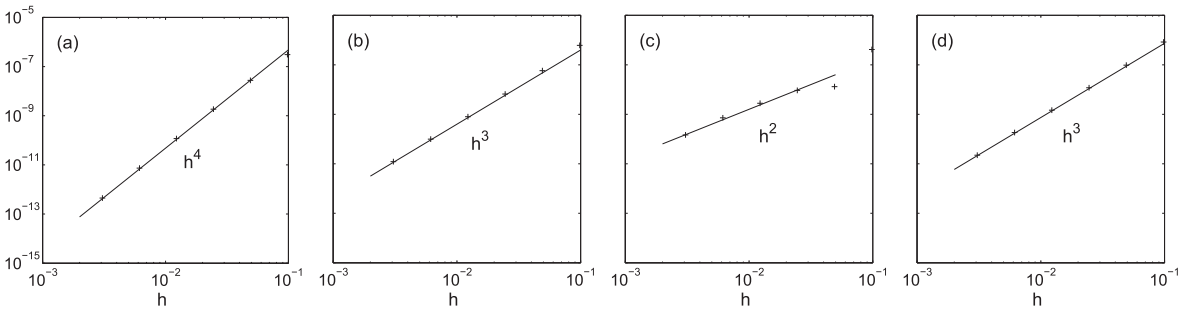

Fig. 3. Maximal approximation error near the axis, $\max_{\alpha_j \approx 0,\pi} |E_5[G]^h_{|[0,\pi]}(\alpha_j)|$ for (a) G^{us}, (b) G^{vs}, (c) G^{ud} and (d) G^{vd}, as given in (2.10) with $u(\alpha) = \sin\alpha$, $v(\alpha) = \cos\alpha$. The data (+) and lines with the indicated slopes (−) are shown.

and then writing

$$I'_{50} = \frac{4}{c^5} E'_{5/2}, \tag{3.14a}$$

$$I'_{51} = \frac{4}{c^5} a \left[b E'_{5/2}(k) - E_{3/2}(k) + \frac{2}{3(1-k^2)} \right], \tag{3.14b}$$

etc. The functions Q_{ik} are then computed by replacing the I_{jk} by I'_{jk} and reorganizing the components containing F_{sing}. For example, Q_{11} is computed as follows:

$$Q^u_{11} = -6x[x^3 I'_{51} - x^2 x_j (I'_{50} + 2I'_{52}) + x x_j^2 (I'_{53} + 2I'_{51}) - x_j^3 I'_{52} + (x - x_j)^3 F_{sing}], \tag{3.15}$$

and similarly for the other Q_{ik}'s.

The reduction in roundoff error is thus obtained by replacing the factor multiplying F_{sing}, which is $x^3 - 3x^2 x_j + 3x x_j^2 - x_j^3$, by $(x - x_j)^3$. A simple MATLAB experiment illustrates the difference between the two [38, Section 1.4.3]. Fig. 4(a) and (b) plots $y = (x-1)^3$ and $y = x^3 - 3x^2 + 3x - 1$ respectively, vs. $x - 1$, computed in MATLAB. While the graph in (a) is monotonic, the graph in (b) has roundoff error of order 10^{-15} introduced by cancellation. This error is small, but is amplified by the large values of the factor F_{sing}. For example, if $x = 1,\ x - x_j = 0.01$ and $y = y_j$, then $F_{sing} \approx 1.1 \times 10^9$ and the errors of order 10^{-15} are amplified to be of order 10^{-6}. This illustrates how fast F_{sing} grows as $(x, y) \to (x_j, y_j)$, and amplifies the small numerical error between $(x - x_j)^3$ and $x^3 - 3x^2 x_j + 3x x_j^2 - x_j^3$.

The result of the proposed change in the computation of the Q's is shown in Fig. 5. The figure shows the errors obtained after replacing (3.9) by (3.15) and similarly for all other Q's. (It also includes the removal of large errors near the poles described in the next section.) Notice that the roundoff error noise in the double layer integrals has been reduced from 10^{-7} (Fig. 2(c) and (d)) to 10^{-13} (Fig. 5(c) and (d)). While the noise is still larger than that in the single layer integrals (Fig. 5(a) and (b)), it is sufficiently low for the method to be used in practical applications that require high accuracy.

3.3. Removing loss of accuracy near poles

The degeneracy of the error near the poles is similar to the one observed for axi-symmetric vortex sheets in Eulerian flows [3,12,29,22–24] and Darcian flows [9]. It is caused by the unbounded behaviour of the derivatives of G at the poles and the coefficients c_k as $\alpha_j \to 0, \pi$. For example, using arguments similar to those in Nitsche [23,24], one can show that

$$c_k^{ud} \sim \frac{1}{\alpha_j^{k-1}}, \quad \text{as } \alpha_j \to 0. \tag{3.16}$$

Substituting this expression into (3.5) and (3.6) with $\alpha_j = h$ it is clear that the term $c_2(\alpha_j, t)h^3$ as well as all other terms involving $c_k(\alpha_j, t)$ are of order $O(h^2)$. Eq. (3.16) also explains why the error is the largest when $j = 1$. We remark that without the single layer desingularization the behaviour of all coefficients at the poles is more singular, and would yield maximal errors of order $O(h)$. For this reason the simple trapezoidal rule T_2 requires the desingularization to be uniformly of second order.

One goal of this paper is to obtain a uniformly accurate fifth order approximation for the integrals of G. We achieve this by finding a pole correction to the proposed quadrature (3.5) using the ideas developed in Nitsche [23,24] for inertial vortex sheets. The corrections are obtained using sufficiently good approximations B of the integrands G that capture the singular behaviour of G at the poles. These approximations are obtained using Taylor series expansions. We then approximate

$$\int G = \int (G - B) + \int B \approx T_5[G - B] + \int B = T_5[G] + E_5[B]. \tag{3.17}$$

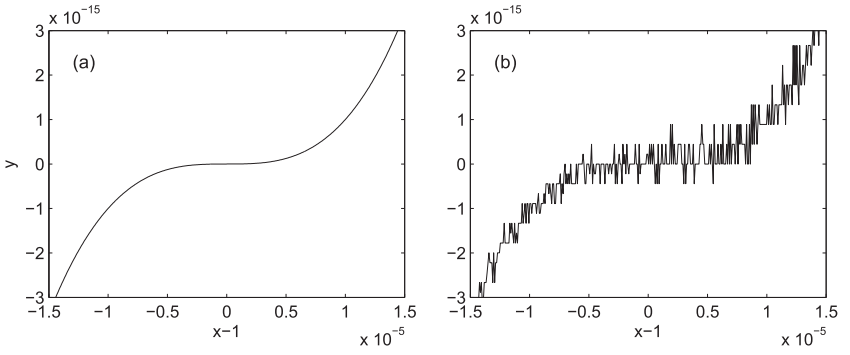

Fig. 4. MATLAB results for y, plotted vs. $x - 1$, where (a) $y = (x-1)^3$, (b) $y = x^3 - 3x^2 + 3x - 1$.

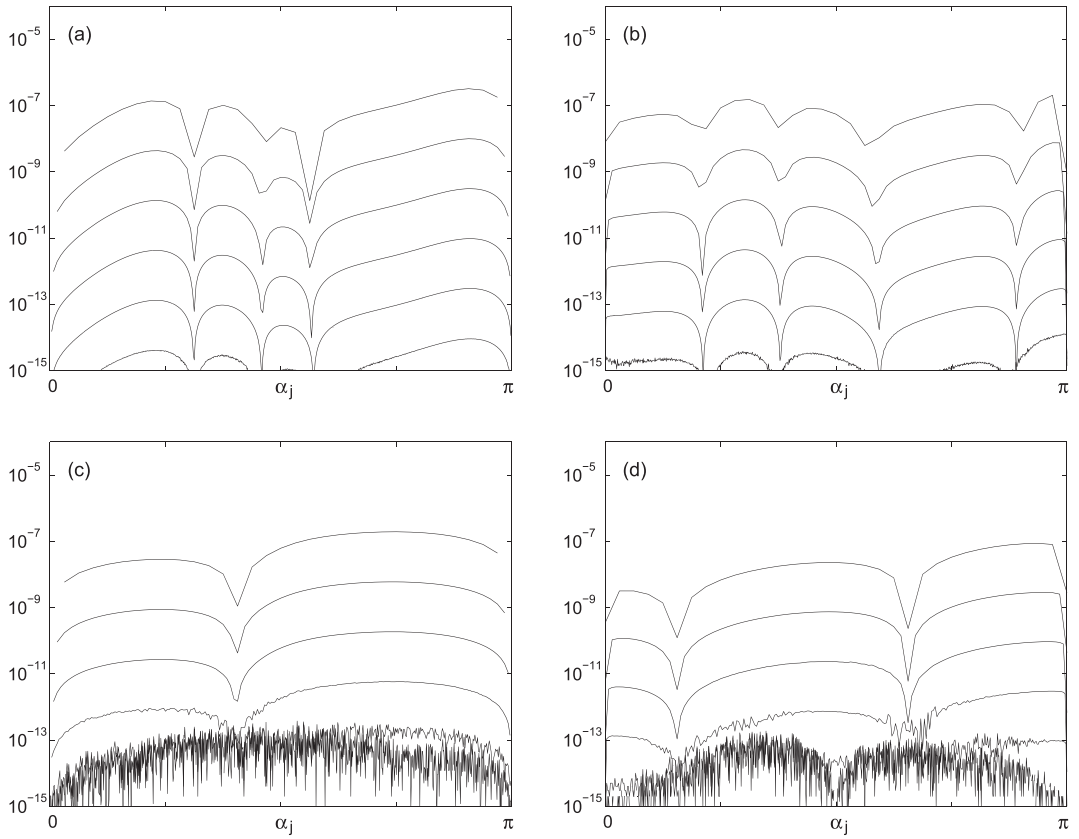

Fig. 5. Approximation error $E_{5u}[G]^h_{[0,\pi]}$ vs. α_j, for $h = \pi/N$ with $N = 32, 64, 128, 256, 512, 1024$, and (a,b,c,d) G^{us}, G^{vs}, G^{ud} and G^{vd}, respectively, replacing u, v by $\sin\alpha$, $\cos\alpha$.

Since $G - B$ is less singular than G, the integral $\int(G - B)$is computed more accurately. It turns out that the corrections $E_5[B]$ can be essentially precomputed and added to T_5 at minimal cost per timestep. This, in a nutshell, is the main idea of this section. Some of the details necessary to understand the method are given next, and all values necessary to implement it are given in the appendices. The corrections and a sample code can also be obtained by emailing the corresponding author.

To approximate G near the left endpoint we use Taylor series about $\alpha, \alpha_j \approx 0$. The symmetry of the interface across the axis implies that

$$\begin{aligned} x(\alpha,t) &= \dot{x}_0(t)\alpha + \frac{\dddot{x}_0(t)}{6}\alpha^3 + O(\alpha^5),\\ y(\alpha,t) &= y_0(t) + \frac{\ddot{y}_0(t)}{2}\alpha^2 + O(\alpha^4),\\ \kappa(\alpha,t) &= \kappa_0(t) + \frac{\ddot{\kappa}_0(t)}{2}\alpha^2 + O(\alpha^4) \end{aligned} \tag{3.18}$$

with similar expansions for $x(\alpha_j,t)$, $y(\alpha_j,t)$, and $\kappa(\alpha_j,t)$. We expand the functions $M(x,x_j,\xi)$ and $Q(x,x_j,\xi)$, where $\xi = y - y_j$, about the base point $\mathbf{p} = (\dot{x}_0\alpha, \dot{x}_0\alpha_j, 0)$. For example,

$$\begin{aligned} M(x,x_j,\xi) = M(\mathbf{p}) &+ \frac{\partial M}{\partial x}(\mathbf{p})\left(\frac{\dddot{x}_0(t)}{6}\alpha^3 + \cdots\right) + \frac{\partial M}{\partial x_j}(\mathbf{p})\left(\frac{\dddot{x}_0(t)}{6}\alpha_j^3 + \cdots\right) + \frac{\partial M}{\partial \xi}(\mathbf{p})\left(\frac{\ddot{y}_0(t)}{2}(\alpha^2 - \alpha_j^2) + \cdots\right)\\ &+ \frac{\partial^2 M}{\partial \xi^2}(\mathbf{p})\left(\frac{\ddot{y}_0^2(t)}{8}(\alpha^2 - \alpha_j^2)^2 + \cdots\right) + \frac{\partial^2 M}{\partial \xi \partial x}(\mathbf{p})\left(\frac{\ddot{y}_0(t)\dddot{x}_0(t)}{12}(\alpha^2 - \alpha_j^2)\alpha^3 + \cdots\right) + \cdots \end{aligned} \tag{3.19}$$

We then substitute these expansions into the integrands (2.10) and obtain the approximations near the left endpoint. The approximations near the right endpoint are obtained similarly. The number of terms needed in the Taylor expansions is determined by the desired order of accuracy and the dependence of derivatives of M, Q on α_j. For uniform fifth order quadratures, we need fourth order approximations of G. Furthermore, we observed that the kth derivatives of M and Q behave as $O(1/\alpha_j^k)$ and $O(1/\alpha_j^{k+1})$, respectively. These observations determine the number of terms needed. For example, fourth order

approximations of G require 14 terms in the expansion of Q_{11}. In principle, following this script one can find arbitrarily high order approximations, as needed to obtain higher order uniform quadratures.

The results, obtained with Mathematica, are that

$$G^{us} = B^{l,us}(\alpha, \alpha_j, t) + O(\alpha^5, \alpha_j^5), \tag{3.20a}$$

$$G^{vs} = B^{l,vs}(\alpha, \alpha_j, t) + O(\alpha^4, \alpha_j^4), \tag{3.20b}$$

$$G^{ud} = B^{l,ud}(\alpha, \alpha_j, t) + O(\alpha^5, \alpha_j^5), \tag{3.20c}$$

$$G^{vd} = B^{l,vd}(\alpha, \alpha_j, t) + O(\alpha^4, \alpha_j^4), \tag{3.20d}$$

where

$$B^{l,us}(\alpha, \alpha_j, t) = \alpha_j^3 b_1^{l,us}(t) B_1^{us}(\eta), \tag{3.21a}$$

$$B^{l,vs}(\alpha, \alpha_j, t) = \alpha_j^2 b_1^{l,vs}(t) B_1^{vs}(\eta), \tag{3.21b}$$

$$B^{l,ud}(\alpha, \alpha_j, t) = \alpha_j b_1^{l,ud}(t) B_1^{ud}(\eta) + \alpha_j^3 \sum_{k=2}^{6} b_k^{l,ud}(t) B_k^{ud}(\eta), \tag{3.21c}$$

$$B^{l,vd}(\alpha, \alpha_j, t) = \alpha_j^2 \sum_{k=1}^{2} b_k^{l,vd}(t) B_k^{vd}(\eta), \tag{3.21d}$$

$\eta = \alpha/\alpha_j$, and the functions $b^l(t)$ and $B(\eta)$ are as given in Appendix D. The approximations of G near the right endpoint are identical, except that at all places in (3.21) α and α_j are replaced by $\alpha - \pi$ and $\alpha_j - \pi$, respectively, and superscripts l are replaced by r, with $b^r(t)$ also given in Appendix D. The functions $b^l(t)$ and $b^r(t)$ depend on derivatives of $x,\ y,\ \kappa,\ u,\ v$ at the endpoints. Details of these functions will be important to understand the impact of the corrections in applications, and will be discussed later, in Section 4.

What is notable in the approximations (3.21) is that the coefficients $b_k(t)$ are independent of j and the functions $B_k(\eta)$ are independent of time. This implies that the corrections $E[B]$ can basically be precomputed. The terms $E[B_k]$ can be precomputed at time $t = 0$, and at each timestep, the corrections can be found solely by computing the coefficients $b_k(t)$ at a cost of $O(1)$.

Some small details remain to be explained. For convenience, we compute the integration error $E[B]$ in (3.17) over an interval proportional to α_j of the form $[0, L\alpha_j]$. We choose $L = 10$, which is sufficiently large to cover the range in which B approximates G well. Following the outline (3.17) we obtain

$$\int_0^\pi G\, d\alpha \approx T_5[G]_{[0,\pi]}^h + E[B^l]_{[0,10\alpha_j]}^h. \tag{3.22}$$

The numbers $E[B]$ are the pole corrections to our original approximation. Since for any function $f(\alpha, \alpha_j, t)$, $E[f]_{[0,10\alpha_j]}^h = \alpha_j E[f]_{[0,10]}^{1/j}$ it follows that

$$E[B^{l,us}]_{[0,10\alpha_j]}^h = \alpha_j^4 b_1^{l,us}(t) E[B_1^{us}]_{[0,10]}^{1/j}, \tag{3.23a}$$

$$E[B^{l,vs}]_{[0,10\alpha_j]}^h = \alpha_j^3 b_1^{l,vs}(t) E[B_1^{vs}]_{[0,10]}^{1/j}, \tag{3.23b}$$

$$E[B^{l,ud}]_{[0,10\alpha_j]}^h = \alpha_j^2 b_1^{l,ud}(t) E[B_1^{ud}]_{[0,10]}^{1/j} + \alpha_j^4 \sum_{k=2}^{6} b_k^{l,ud}(t) E[B_k^{ud}]_{[0,10]}^{1/j}, \tag{3.23c}$$

$$E[B^{l,vd}]_{[0,10\alpha_j]}^h = \alpha_j^3 \sum_{k=1}^{2} b_k^{l,vd}(t) E[B_k^{vd}]_{[0,10]}^{1/j}. \tag{3.23d}$$

Note that for $\alpha_j = h$ ($j = 1$), the corrections (3.23a–d) are $O(h^4),\ O(h^3),\ O(h^2)$ and $O(h^3)$, respectively, in agreement with the numerical results in Fig. 3.

The time-independent factors $E[B_k^l]_{[0,10]}^{1/j}$ are precomputed at $t = 0$. Since the integration interval for B was chosen proportional to α_j, these factors depend only on j and not on h, and can conveniently be precomputed once for all meshes to be used.

Finally, to obtain uniformity near the right endpoint we need to add corrections at the right, using the functions B_r given by (3.21), as described earlier. Both left and right corrections are incorporated into the final approximation, which we label T_{5u}, as follows:

$$\int_0^\pi G\, d\alpha \approx T_{5u}[G] = T_5[G]_{[0,\pi]}^h + w_1(\alpha_j) E_5[B^l]_{[0,10\alpha_j]}^h + w_2(\alpha_j) E_5[B^r]_{[\pi-10\alpha_j,\pi]}^h, \tag{3.24}$$

where the weights w_1 and w_2 are positive functions that equal one at the left or right endpoint, are smooth, and vanish sufficiently fast away from that endpoint. Details of these functions are not critical, but for smoothness we have chosen either $w_1 = \cos^8\left(\frac{\alpha_j}{2}\right) / \left(\sin^8\left(\frac{\alpha_j}{2}\right) + \cos^8\left(\frac{\alpha_j}{2}\right)\right)$ and $w_2 = \sin^8\left(\frac{\alpha_j}{2}\right) / \left(\sin^8\left(\frac{\alpha_j}{2}\right) + \cos^8\left(\frac{\alpha_j}{2}\right)\right)$ or a rescaled Erfc function as proposed in [7, Eq. (22)], when faster decay away from the endpoint is needed. The Erfc function decays smoothly from 1 to 0 over a finite interval.

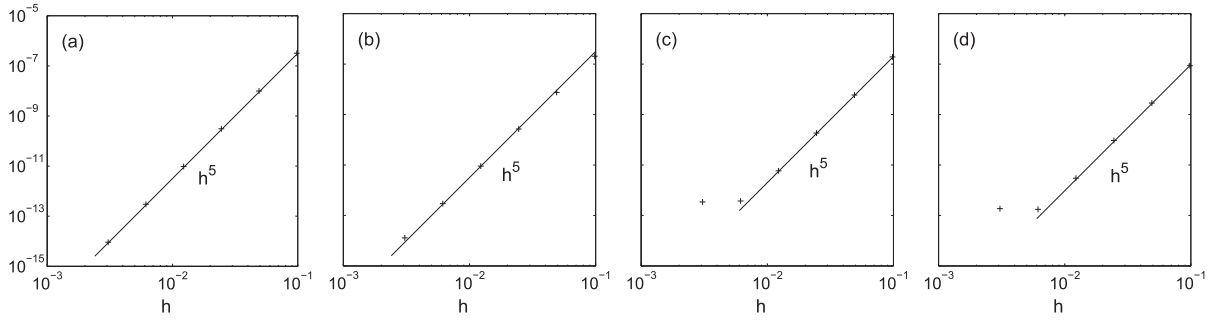

Fig. 6. Maximal approximation error $\max_{\alpha_j\in[0,\pi/2]}|E_{5u}[G]^h_{[0,\pi]}(\alpha_j)|$ vs. h, for G equal to (a) G^{us}, (b) G^{vs}, (c) G^{ud}, (d) G^{vd}, as given in (2.10) with $u(\alpha)=\sin\alpha$, $v(\alpha)=\cos\alpha$. The data (+) and lines with the indicated slopes (−) are shown.

All values c_k, $\widetilde{B}_k(\alpha_j,\alpha_j,t)$, and derivatives of B_k needed to compute $E[B_k]$ are given in Appendix E for the single layer, as illustration. The numbers $E[B_k]^{1/j}$ are computed in quadruple precision to reduce the effect of roundoff error.

The resulting approximation error after including the corrections, $E_{5u}[G]^h_{[0,\pi]}$, is plotted in Fig. 5 as a function of α_j. Observe that the large errors near the poles have been eliminated. To confirm that the approximation is now uniformly fifth order, Fig. 6 plots the maximal error as a function of h on a log–log scale (+) together with a line of slope 5 (−). Comparison with Fig. 3 shows the improvement obtained with the pole corrections. The data in Fig. 6 confirms that the corrected method T_{5u} is uniformly of fifth order.

4. Computing the interface evolution

4.1. Numerical method

This section applies the quadrature rules developed in Section 3 to compute the evolution of three sample flows. For the computations, we found it convenient to use the arclength-tangent angle framework proposed by Hou et al. [17], which is briefly described next.

Note that the evolution of the interface $\mathbf{x}(\alpha,t)$ is uniquely determined by its *normal* velocity. That is, for an interface tracked by Lagrangian particles marked by α, the tangential velocity of these particles does not alter the interface position, it only alters the position of the marker particles along the interface. With this in mind, given initial conditions, the interface $\mathbf{x}(\alpha,t)$ is determined by

$$\frac{\partial\mathbf{x}}{\partial t}=\mathbf{u}+T\mathbf{s}, \tag{4.1}$$

where $\mathbf{u}(\alpha,t)$ is given by (2.4), $\mathbf{s}(\alpha,t)$ is the unit tangent vector to the sheet, and $T(\alpha,t)$ can be chosen arbitrarily.

If $T=0$, the Lagrangian particles generally accumulate near isolated points on the interface, which in certain cases impacts the numerical stability of the discretization. Following Hou et al. [17], we instead choose T so as to control where and when the Lagrangian marker particles accumulate. For simplicity, here we choose T so that the particles remain equally spaced in arclength. Alternative choices are possible, see, for example [17, Appendix]; [25].

To proceed, it is convenient to rewrite Eq. (4.1) in terms of the tangent angle $\theta(\alpha,t)$ and the relative spacing between points s_α, where $s(\alpha,t)$ is arclength. Here and below, the subscripts α and t denote partial differentiation with respect to that variable. The variables θ and s_α are related to x and y by

$$x_\alpha=s_\alpha\cos\theta,\quad y_\alpha=s_\alpha\sin\theta, \tag{4.2}$$

where $x(0,t)=0$ and $y(0,t)=y_0(t)$. In the equal arclength case the relative spacing between points is constant in α, and thus $s_\alpha=L(t)/\pi$, where L is the length of the curve in the cross-section. Using these variables, Hou et al. [17] showed that (4.1) is equivalent to

$$L_t=-\int_0^\pi\theta'_\alpha U\,d\alpha',\quad \theta_t=\frac{\pi}{L}(U_\alpha+\theta_\alpha\widetilde{T}),\quad (y_0)_t=v(0,t), \tag{4.3}$$

where $U=\mathbf{u}\cdot\mathbf{n}$, $\mathbf{n}$ is the outward unit normal, and $\widetilde{T}(\alpha,t)=\alpha L_t/\pi+\int_0^\alpha\theta'_\alpha U\,d\alpha'$. The relation to T is that $\widetilde{T}=\mathbf{u}\cdot\mathbf{s}+T$.

The numerical method used in the following sections consists of discretizing the interface by $N+1$ points uniformly spaced in the Lagrangian variable α, $\theta_j(t)\approx\theta(\alpha_j,t)$, where $\alpha_j=jh$, $h=\pi/N$, $j=0,\dots,N$, with total length $L(t)$ and intersecting the axis at $(0,y_0(t))$. The variables L, θ_j and y_0 satisfy a system of ordinary differential equations obtained by approximating all derivatives in (4.3) spectrally and all integrals to sixth order using the modified trapezoidal rule. The velocity $\mathbf{u}$ is computed either to second order with T_2 (3.3), to pointwise fifth order with T_5 (3.5), or to uniform fifth order with T_{5u} (3.24). For $\lambda\neq1$, the Fredholm integral equation for $\mathbf{u}$ is solved using GMRES [16] with a prescribed residual tolerance of

10^{-13}. The system is integrated in time using the fourth order Runge–Kutta method. Here, the initial condition must satisfy that s_α be constant.

4.2. Finite time pinchoff

The first example consists of the initial condition

$$\theta_j(0) = \alpha_j + \left(\frac{2}{3} + 5a\right)\sin(2\alpha_j) + \left(\frac{1}{12} + 4a\right)\sin(4\alpha_j) + a\sin(6\alpha_j) \tag{4.4}$$

with $L(0) = \pi$ and $y_0(0)$ such that $y_0 = -y_n$ for symmetry, in zero external flow, $\mathbf{u}^\infty = 0$, and with viscosity ratio $\lambda = 0.1$. Eq. (4.4), proposed by Almgren [2], describes a dumbbell for an approximate range of values $0.016 \leqslant a \leqslant 0.099$. We choose $a = 0.09$. Note that by prescribing initial values for θ_j, L and y_0 (instead of x and y) the initial condition is implicitly equally spaced in arclength.

Fig. 7 shows the solution at a sequence of times $0 \leqslant t \leqslant 0.82$, computed with the uniform fifth order rule T_{5u}, using $N = 2048$ and $\Delta t = 0.000625$ sufficiently small that the temporal discretization error is smaller than the spatial one. For these parameters, the execution time was 1.4 h on a 2.4 GHz desktop. The arrow in Fig. 7(a) indicates the direction of increasing time. The interface, which evolves solely based on its initial curvature distribution, appears to pinch at two symmetric points. Fig. 7(b) shows a closeup near the upper pinchoff point. The minimum radius near this point is shown in Fig. 8 as a function of time. Fig. 8(a) plots the result using the parameters of Fig. 7. It shows that after an initial time, the radius approaches zero almost linearly in time, indicating finite time pinchoff. The smallest radius computed with $N = 2048$ is $r_{min} = 0.0005$ and the corresponding maximal curvature is $\kappa_{max} = 1800$. Fig. 8(b) shows a closeup of the results computed with $N = 2048$ (—), 1024 (---), 512 (-·). The three data sets appear almost linear, and overlap closely with each other, until toward the last times, when the lower resolution data begin to oscillate.

We estimate the pinchoff time by approximating the $N = 2048$ data by a least squares linear polynomial over the interval [0.76,0.81]. This line is plotted in figure (b) over a small time-interval $t \in [0.822, t_c]$, where $t_c = 0.8258$ is the time at which it crosses the t-axis. The line agrees with the data over the interval of approximation to within $\times 10^{-5}$, and cannot be distinguished visually from it at this scale, which is why it is only plotted on a small time interval near t_c. By varying the domain used for the least squares approximation and comparing linear and quadratic approximations, we estimate that t_c approximates the pinchoff time within ± 0.0002. This figure thus indicates finite time pinchoff and the accuracy obtained with the fifth order method at the given resolutions.

Fig. 9 compares the results using different methods. It plots the solution at a sequence of times near pinchoff using the second order quadrature T_2 (---) and the uniformly fifth order quadrature T_{5u} (—), with $N = 512$ in figure (a) and $N = 1024$ in figure (b). The last times shown in each case are those times past which the second order method no longer converges. It shows that the differences between the two methods increases significantly as $t \to t_c$, and suggests that for a given meshsize, the higher order method resolves the solution near pinchoff significantly better.

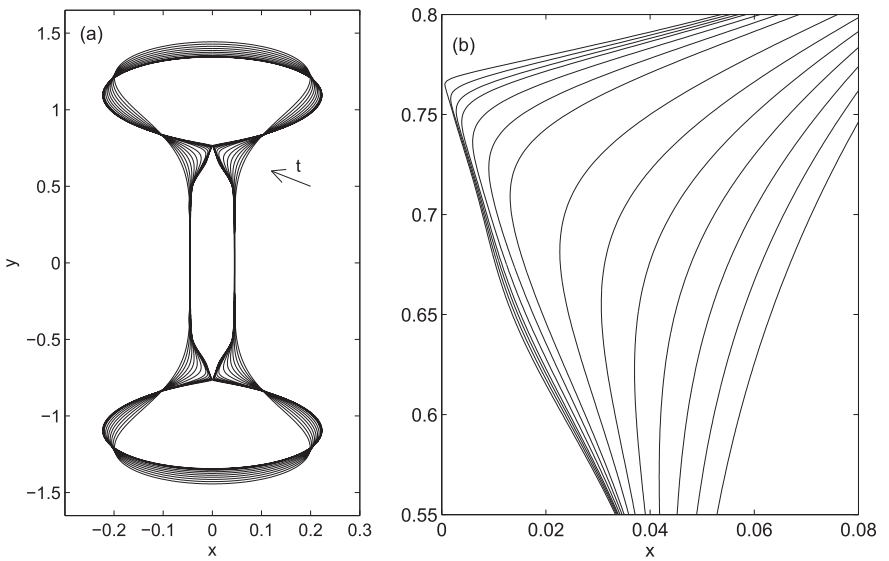

Fig. 7. Evolution of the dumbbell-shaped bubble (4.4) with $a = 0.09$, $Ca = 0$, and $\lambda = 0.01$, computed using T_{5u} with $N = 2048$ points. The solution is shown at times t = 0.0:0.1:0.7, 0.74, 0.77, 0.79:0.01:0.82. (a) The arrows indicate the direction of motion as time increases. (b) Closeup near pinchoff.

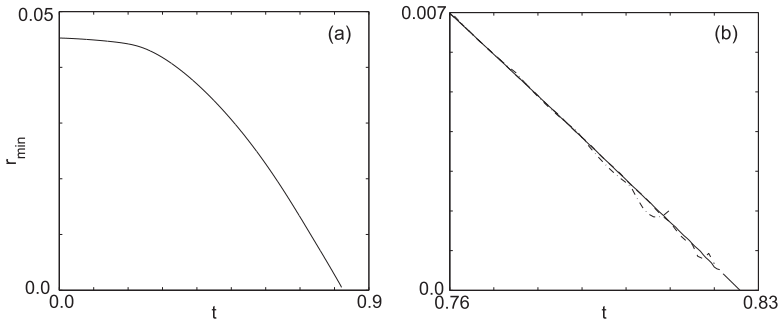

Fig. 8. Minimum radius vs. time. (a) Computed using $N = 2048$. (b) Closeup showing results with $N = 2048$ (—), $N = 1024$ (---), $N = 512$ (-·). The dotted line shown on $t \in [0.821, t_c]$, $t_c = 0.8258$ is obtained by a linear least squares fit of the $N = 2048$ data over $t \in [0.76, 0.81]$.

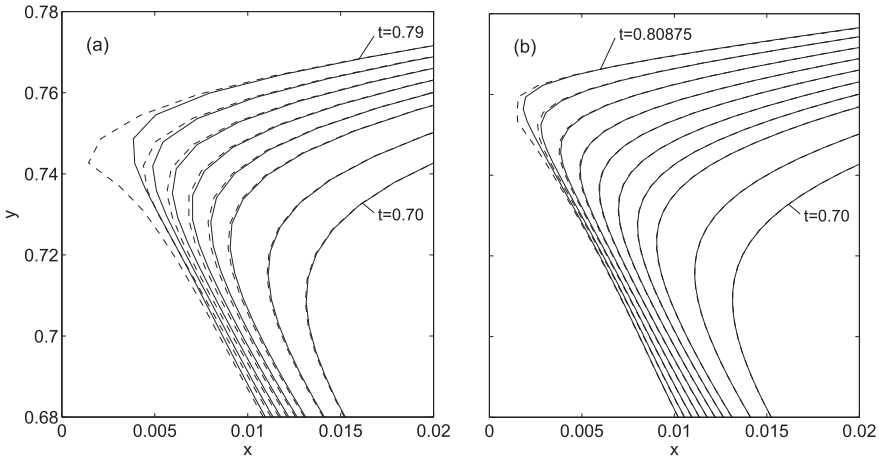

Fig. 9. Closeup of solutions near pinchoff time computed with (a) $N = 512$, (b) $N = 1024$, using the second order method (---) and the uniformly fifth order method (—), at times ranging from the smallest to the largest times indicated in the figures.

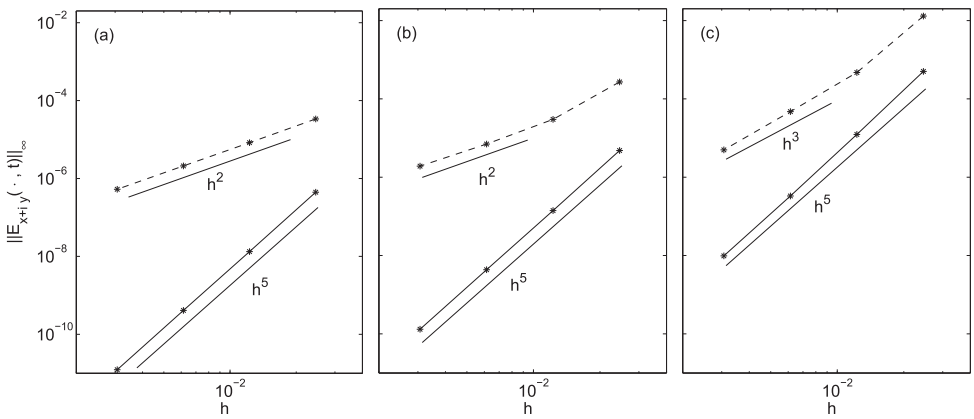

Fig. 10. Maximal errors in the position $x + iy$ vs. $h = \pi/N$, at fixed time (a) $t = 0.1$, (b) $t = 0.4$, (c) $t = 0.7$, using the second order method (---) and the uniformly fifth order method (—).

To more accurately compare the methods, Fig. 10(a)–(c) plots the maximal l_2 errors in the position at times $t = 0.1$, 0.4, and 0.7, respectively, vs. $h = \pi/N$, where $N = 128$, 256, 512, 1024. The errors are obtained by comparing the solution to the fifth order results with $N = 2048$. The lines have the indicated slopes. They show that the fifth order method converges as $O(h^5)$ at all times, and that the errors are much smaller than the ones with the second order method.

The maximal errors shown in Fig. 10 increase in time. For the second order method, the errors increase slightly, and the $O(h^2)$ terms become dominated by $O(h^3)$ terms in Fig. 10(c). This can be understood by investigating the pointwise second and third order terms in the error, as given in (3.1). The second order terms are those containing first derivatives of G at the endpoints. These derivatives are given in equations (C3, C7, C11, C15) and depend on zeroth derivatives of curvature and velocities. The third order term in (3.1) is the one containing c_2, which, as listed in (C2, C6, C10, C14), depends on second derivatives of curvature. Since higher derivative grow faster as the curvature grows near pinchoff, the third order terms soon dominate the second order ones. For the fifth order method, the errors remain $O(h^5)$ throughout, but increase significantly due to the increasing curvature and its derivatives.

The time evolution of the error is more clearly shown in Fig. 11, which plots the maximal error using $N = 512$ and $N = 1024$ as a function of time, for all times before GMRES no longer converges. Fig. 11(a) shows that the error increases as pinchoff is approached. The difference between the two methods decreases on a logarithmic (but not on a linear) scale. However, as shown in the closeup in Fig. 11(b), for equal resolution N, the fifth order method is still about 50 times more accurate at the time the second order method breaks down. It furthermore solves the equations for longer times. Thus the fifth order method more accurately resolves the solution at times more closely to pinchoff, as is already indicated in Fig. 7.

To determine the effect of the local corrections required for uniformity, Fig. 12 compares the pointwise and uniform fifth order methods. Figures (abc) plot the l_2 error in the computed position as a function of α/π, using N = 128, 256, 512, 1024, at a sequence of times t = 2, 6 and 10, respectively. The error without corrections (using T_5) is shown as the dashed curve, the error with corrections (using T_{5u}) is shown as the solid curve. Initially, the corrections improve the error near the boundary. But at the present resolutions the degeneracy at the axis is small, and the maximum error, which occurs away from the axis, is the same for both methods. As time increases the difference between the two methods decreases, until at $t = 10$ there is no difference on the whole domain. Thus, in this case the corrections required in theory for uniformity do not affect the maximum error in practice. This can be understood by investigating the coefficients $b_k(t)$ multiplying the constants $E[B](j)$, given in Appendix D. Notice that unlike the values of c_2 or $\partial G/\partial\alpha$, the coefficients $b_k(t)$ depend on derivatives of the curvature and velocities at the endpoints only. As the dumbbell evolves the curvature at the endpoint approaches a constant, and the endpoint velocities decay to zero. Thus in this application the corrections are relatively small and decrease in time, and would only be significant at much higher resolutions than the ones we used. This example illustrates how the specific form of the b_k's can be used to determine whether or not the corrections are needed to improve the results in a given applications.

In summary, this example of finite time pinchoff is significantly better resolved by the fifth order method. However, the pole corrections required in theory for uniformity are negligible since the flow velocities and the changes in curvature at the poles vanish.

4.3. Steady bubbles in a strainflow

For our next example, we consider a case in which the spatial changes in the curvature at the poles do not vanish in time. The example is the initially spherical bubble

$$\theta_j(0) = \alpha_j, \quad L(0) = \pi, \quad y(0) = -1, \tag{4.5}$$

in the axi-symmetric strain field (see [40]),

$$\frac{2Ca}{1+\lambda}\mathbf{u}_\infty = \frac{Ca}{1+\lambda}(-x, 2y). \tag{4.6}$$

Taylor [37] reported experimental results in which a drop is placed in a flow produced by four counter-rotating rollers. He found that for strain rates less than a critical value, $Ca < Ca_{cr}(\lambda)$, the drops first elongate and then approach a steady state. This was also observed in time-dependent numerical simulations by Rallison and Acrivos [31]. Pozrikidis [27] computed the

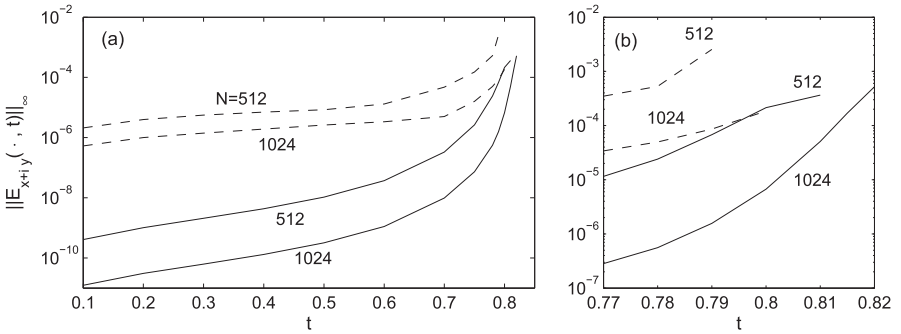

Fig. 11. Maximal errors in the position $x + iy$ vs time, using the second order method (---) and the uniformly fifth order method (—). Two curves are shown for each method, obtained with $N = 512$ and $N = 1024$ respectively. (b) is a closeup of (a).

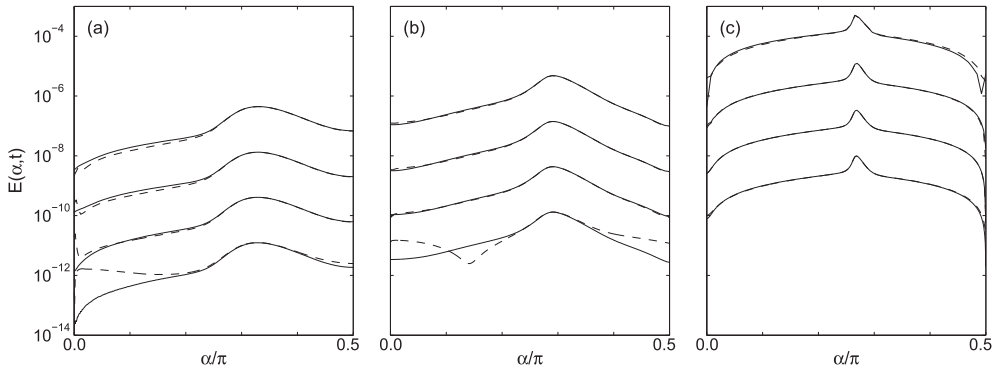

Fig. 12. Errors in the position $(x+iy)(\alpha,t)$ as a function of α, using the pointwise fifth order method T_5 (---) and the uniformly fifth order method T_{5u} (—), at (a) $t=0.1$, (b) $t=0.4$, (c) $t=0.7$. The four curves shown for each method correspond to N = 128, 256, 512, and 1024, and are computed by comparing to the uniformly fifth order approximation with $N=2048$.

time-dependent evolution as well and found some steady states using a more general background strainfield. Eggers and du Pont [13] recently found steady solutions numerically by solving time-independent equations iteratively with Newton's method. They found stable and unstable steady states as well as critical capillary numbers for a range of values of λ. Our goal here is to investigate the performance of the three methods $T_2,\ T_5,\ T_{5u}$ to compute the time evolution of the drop, as illustrated by one sample case.

In these simulations it is important that volume be well conserved, since any small errors in the volume are quickly amplified by the background strain flow. Volume conservation can be achieved either by using extremely small timesteps or by specifying the length L at each time so that the current volume equal the initial volume, $4\pi/3$. We found that with this latter approach the results converged significantly faster under timestep refinement. We therefore used this method to compute $L(t)$ instead of solving the ordinary differential equation (4.3) for L_t explicitly.

Fig. 13 plots the solution for $\lambda=0.01$ and $Ca=0.20$, computed with T_{5u} using $N=1024$ and $\Delta t=0.005$, at a sequence of times $t=0:2:30$. The computed bubble stretches and appears to approach a steady state. However, it is difficult to determine whether the solution is truly near a steady state since at all times shown in the figure, indeed at any time, the time-dependent solution is changing. This becomes increasingly difficult the closer Ca is to Ca_{cr}.

To obtain more conclusive evidence of convergence to a steady state, we consider the maximum curvature κ_{max}, the maximal axial coordinate y_{max}, and the deformation $D=x_{max}/y_{max}$. These quantities, generically denoted by $Q(t)$, are plotted in Fig. 14(a) vs. time. The slope dQ/dt decreases in time. However, this is not sufficient to conclude convergence or to predict the steady state value. Instead, we consider each of these quantities as a series of changes

$$Q_j = Q_0 + \sum_{k=0}^{j-1} \Delta Q_k, \tag{4.7}$$

where $Q_j = Q(j\Delta t)$ and $\Delta Q_k = Q_{k+1} - Q_k$, and wish to determine wether the series converges to a finite steady state value. Fig. 14(b) plots the ratios $r(k) = \Delta Q_{k+1}/\Delta Q_k$ and shows that for all three quantities, this ratio converges to a common value <1. This shows that the three series converge geometrically for sufficiently large times.

Based on extensive simulations varying Ca and the mesh resolution, we found the ratios $r(k)$ plotted in Fig. 14(b) to be a stronger indicator of convergence than the information plotted in Figs. 13 and 14(a). For example, if the resolution is not

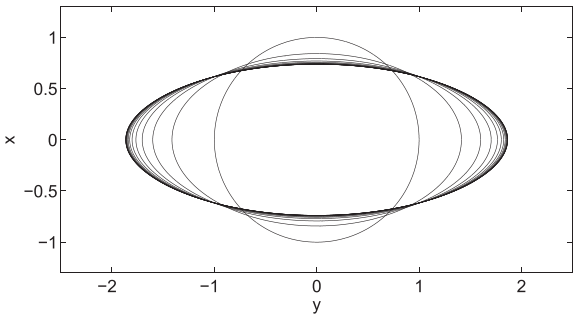

Fig. 13. Evolution of initially spherical bubble in the strainfield (4.6) with $\lambda=0.01$, $Ca=0.20$, using the uniform fifth order method with $N=2048$ points, at times $t=0:2:30$.

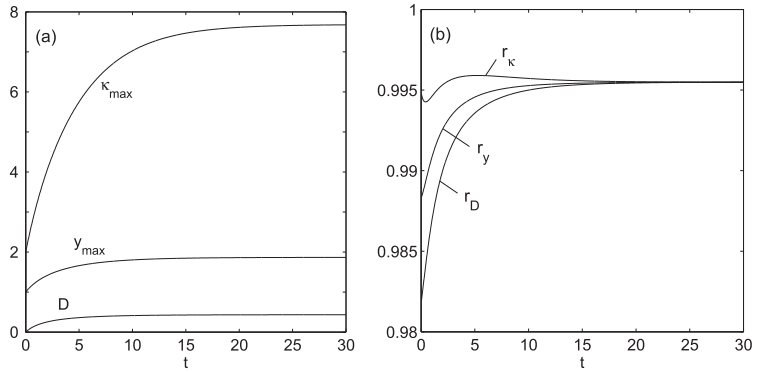

Fig. 14. For the solution presented in Fig. 13, (a) Maximum curvature κ_{max}, maximum y-coordinate y_{max}, and deformation D as vs. time. (b) Ratios $r(k) = \Delta Q_k/\Delta Q_{k+1}$, where $\Delta Q_k = Q_{k+1} - Q_k$, and Q is the maximum curvature (r_κ), the maximum y-coordinate (r_y), and deformation (r_D), vs. time.

sufficient, or if $Ca > Ca_{cr}$, these ratios are the first to depart from a constant common limiting value. Conversely, the fact that all three curves converge to the same value is a strong indicator that the solution is converging towards a steady state, and that it is well resolved. The ratios are thus a good basis on which to compare different methods.

However, the ratios $r(k)$ depend on the timestep used. This is illustrated in Fig. 15(a), which plots the ratio r_y using data sampled at different time intervals $\Delta t = 0.005, 0.01, 0.02$, as indicated. The timestep-dependence is revealed by the following calculation. Note that the limiting value of the ratio r can be used to approximate the steady state values. Assuming that for $k \geqslant j,\ r(k) = r$ is constant (depending only on Δt) then the steady state values are

$$Q_\infty = Q_j + \sum_{k=j}^{\infty} \Delta Q_k = Q_j + \Delta Q_j \sum_{k=0}^{\infty} r^k = Q_j + \frac{\Delta Q_j}{1-r} = Q_j + \frac{\Delta Q_j}{\Delta t}\frac{\Delta t}{1-r} \approx Q_j + \frac{dQ}{dt}\frac{\Delta t}{1-r}. \tag{4.8}$$

Assuming further that Q_j has converged, that is, $Q_j = Q(t_j)$, it follows that $\Delta Q_j/\Delta t = dQ/dt(t_j) + O(\Delta t)$ and thus the dependence of r on Δt is given by

$$\frac{\Delta t}{1-r} = C + O(\Delta t) \tag{4.9}$$

for some constant C. To illustrate, Fig. 15(b) plots the quantity $\Delta t/(1-r)$ using the data spaced at time intervals $\Delta t = 0.005, 0.01, 0.02$, and shows that the three curves collapse onto one. Thus, this timestep-independent quantity is a better characterization of the solution, which converges to a steady state as t increases if $\Delta t/(1-r) > 0$.

Fig. 16(a) and (b) plots the computed values of y_{max}, and the corresponding values $\Delta t/(1-r_y)$, for the second order method T_2 (---) and the fifth order methods $T_5,\ T_{5u}$ (—) with $N = 256$ and 512, as indicated. The second order results quickly depart from the limiting values. This departure is evident at a larger scale in Fig. 16(b). The fifth order results on the other hand have almost converged in N and in time, thus making it possible to accurately determine the steady state using only moderate resolutions. These results show that even for this case of moderate curvatures, much is gained by using the fifth order methods over the second order one.

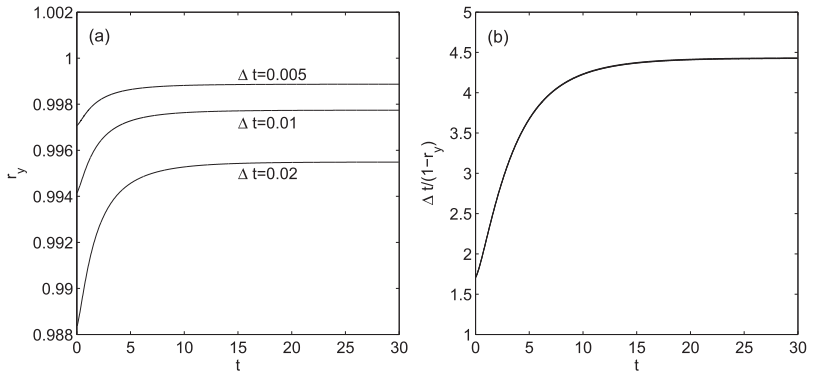

Fig. 15. For the solution presented in Fig. 13, (a) Ratio r_y computed using data spaced at intervals $\Delta t = 0.02, 0.01, 0.005$, as indicated. (b) Quantity $\frac{\Delta t}{1-r(k)}$, using the same three values of Δt. The three curves overlap.

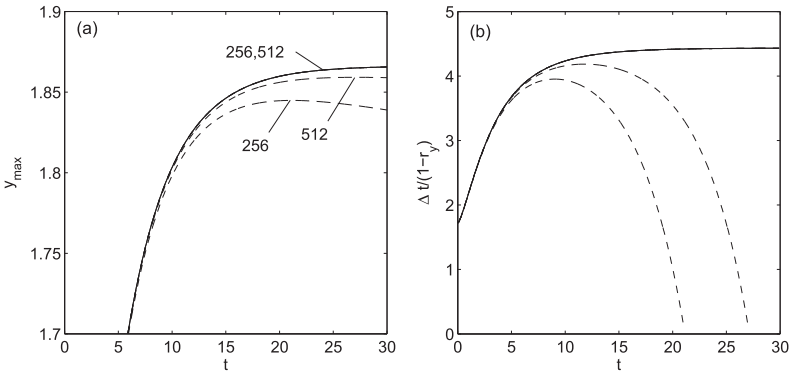

Fig. 16. (a) Maximal y-coordinate y_{max} and (b) values $\Delta t/(1-r_y)$, vs. time, using the second order method (---) and the fifth order methods (—), for $N = 256$ and 512, as indicated.

Fig. 17(a)–(c) compares the maximal errors in the position $x + iy$, obtained with the three methods at $t = 2$, 6 and 10, respectively. The results using T_2 are of second order and increase slightly in time. The results using T_5 and T_{5u} differ slightly in this case. Thus, unlike the results in Fig. 10, here the corrections in T_{5u} improve the maximal error at early times.

Note that at the present resolutions the uncorrected method T_5 has maximal errors of fourth order, and not of second order as may be expected. Again, this can be understood by examining the coefficients $b_k(t)$ of the corrections. According to Appendix D, the maximal second order term in the error is given by

$$b_1^{ud} h^2 E[B^{ud}]^{j=1} = \frac{\nu_0 \ddot{y}_0^2}{\dot{x}_0 |\dot{x}_0|} h^2 E[B^{ud}]^{j=1}. \tag{4.10}$$

Since ν_0 is small and vanishes in these steady state flows, the second order term in the error is negligible. Similarly, all other factors b_k^{ud} and b_k^{vd} depend on pole velocities and its derivatives and are negligible. On the other hand, the fourth and third order terms with coefficients b_k^{us} and b_k^{vs}, respectively, depend on the $\kappa_0''(t)$ which is large, even in this moderate example. Thus one would expect maximal errors of third or fourth order, consistent with the results in figures (a) and (b). However, as time increases the pole curvature grows, and higher derivatives of the curvature grow faster than lower ones. As a result, the fifth order terms in the error, which depends on higher curvature derivatives, grow and soon dominate the maximal error. Thus in this case the pole corrections are insignificant after some time, not because curvature and its derivatives are small, but because they are large.

Note that for sufficiently high resolution, the corrections will improve the error. However, such resolutions appear to be much larger than the ones needed in practice to resolve the curve. Moreover, if the resolution is insufficient to compute the corrections accurately, they worsen the result. This is the reason why in Fig. 17(c) the uncorrected results at low resolutions are slightly better than the corrected results.

In summary, in this example, the fifth order methods are a significant improvement over the second order method, and enable approximating the steady state with moderate resolutions. The corrections however become insignificant relative to higher order terms in the error as the derivatives at the pole grow, and moreover, they become difficult to compute.

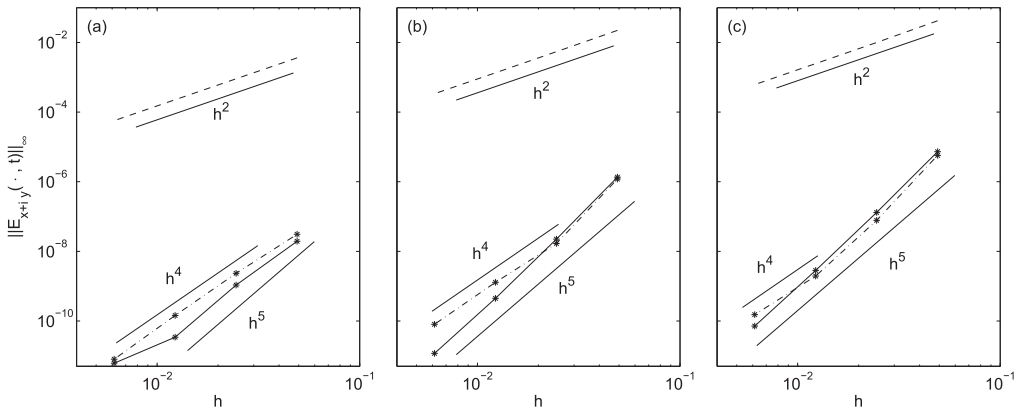

Fig. 17. Maximal errors in the position $x + iy$ vs. $h = \pi/N$, at fixed time (a) $t = 2$, (b) $t = 6$, (c) $t = 10$, using the second order method (---), the pointwise fifth order method (-·-) and the uniformly fifth order method (—).

4.4. Continuously extending drops

For our last example we consider a case in which the pole velocities do not vanish. In such a case the second order error terms in T_5 and the corresponding corrections in T_{5u} could possibly be more significant.

We consider the initial spherical drop (4.5) with $\lambda = 10$, in the external strainfield (4.6) with $Ca = 0.4$. This capillary number is larger than the critical value, which for $\lambda = 10$ is $Ca_{cr} \approx 0.095$ and therefore, the drop is not expected to reach a steady state.

Fig. 18 shows the evolution at uniformly increasing times $t = 0 : 1 : 13$, computed with T_{5u} and $N = 2048,\ \Delta t = 0.005$. Indeed, the solution does not approach a steady state but instead, it continuously extends in the background strainfield. Since the external velocity increases as $|y|$ increases, the drop stretches increasingly fast. As we will explain later, these results are surprisingly difficult to compute, even though the interface is perfectly smooth at all times and maximal curvatures increase only moderately fast.

First, we determine the relative magnitude of the various order error terms in T_5. Fig. 19 plots the evolution of the largest second, third and fourth order terms in (3.23), obtained with $j = 1$, for $n = 128$. That is, it shows

$$d_2(t) = h^2 \left| b_1^{ud}(t) E[B_1^{ud}]^1 \right|, \tag{4.11a}$$

$$d_3(t) = h^3 \max\left(\left| b_1^{vs}(t) E[B_1^{vs}]^1 \right|, \left| \sum_{k=1}^{2} b_k^{vd}(t) E[B_k^{vd}]^1 \right| \right), \tag{4.11b}$$

$$d_4(t) = h^4 \max\left(\left| b_1^{us}(t) E[B_1^{us}]^1 \right|, \left| \sum_{k=2}^{6} b_k^{ud}(t) E[B_k^{ud}]^1 \right| \right). \tag{4.11c}$$

The figure shows that, indeed, initially the second order term, which depends on v_0, is larger than the others. However, as the drop stretches and derivatives of $x,\ y$ grow, so do the higher order terms. As a result, after short time the third order term dominates, and around $t = 8$ the fourth order term dominates. It follows that even though the maximal error in T_5 is $O(h^2)$ at all times, the second order term dominates the error only in a small initial time interval, whose length grows as N increases.

The corrections in T_{5u} remove the low order error terms in T_5 shown in Fig. 19, and the effect of this is shown in Fig. 20. Fig. 20 compares the results using T_2, T_5 and T_{5u}. It plots the maximal curvature vs. time, for several resolutions ranging from $N = 128$, increasing by factors of 2 until $N = 2048$, as indicated. Fig. 20(a) is obtained with T_2, Fig. 20(b) with T_5, and Fig. 20(c) with T_{5u}. These figures illustrate the numerical difficulty in computing the flow. For any method and any set of parameters N and Δt, the results follow the same pattern: as the drop stretches, the maximum curvature increases slowly, but suddenly it becomes unbounded and the computations break down. For example, the second order solution in Fig. 20(a) with $N = 2048$ breaks down around $t = 5$. Notice that at this time the solution plotted in Fig. 18 is smooth and the maximal curvatures are small, ≈ 4, giving no indication of any numerical difficulties. The breakdown time is practically independent of the timestep used, which we varied between $\Delta t = 0.2$ and $\Delta t = 0.0025$. Rallison and Acrivos [31] also observed that for any case with $Ca > Ca_{cr}$, their numerical solutions break down in finite time. They attributed this to a numerical instability related to the physical instability leading to the "bursting" solutions that Taylor [37] observed experimentally.

As shown in Fig. 20, the breakdown time depends on the spatial resolution N, albeit in an unusual non-monotonic fashion. For the second order results in figure (a), the breakdown time *decreases* as N increases from 128 to 2048, which could be misinterpreted as a finite time singularity in the exact solution. For the pointwise fifth order results in figure (b), the breakdown time decreases for low N, but *increases* as N increases past 1024, giving the first indication of convergence as $N \to \infty$ at larger times. For the uniform fifth order results in figure (c), the breakdown time begins to increase already sooner, past $N = 512$. Notice also that the results in (c) solve the equations to largest times.

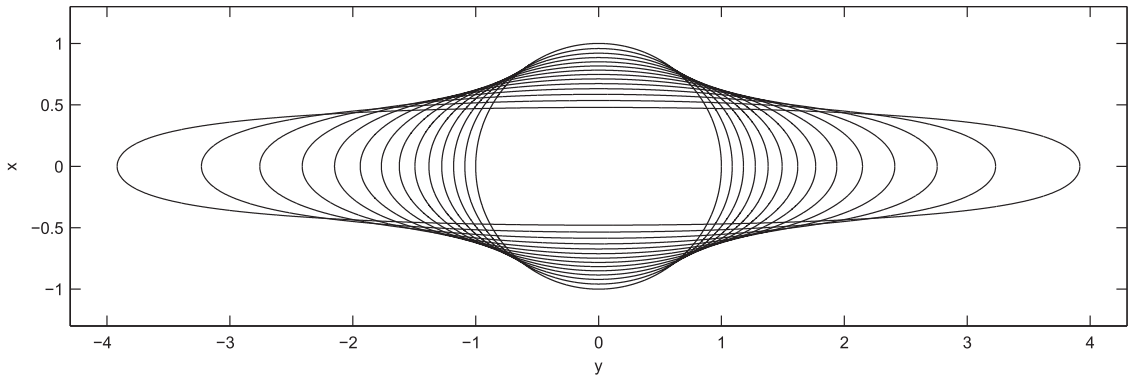

Fig. 18. Evolution of initially spherical bubble in the strainfield (4.6) with $\lambda = 10,\ Ca = 0.40$, at times $t = 0 : 1 : 13$, computed using the uniformly fifth order method with $N = 2048,\ \Delta t = 0.005$.

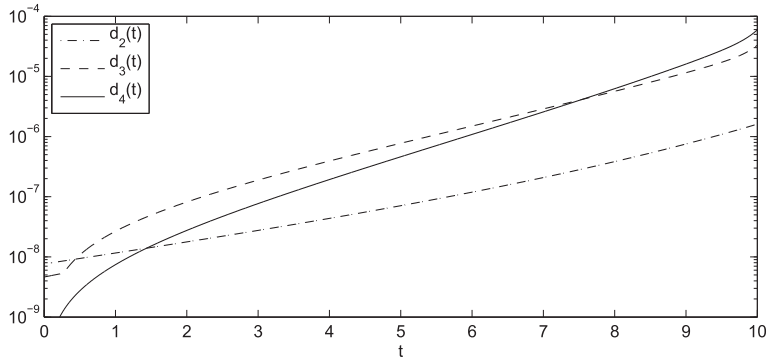

Fig. 19. Largest second, third and fourth order corrections (4.11), $d_2(t)$, $d_3(t)$, $d_4(t)$.

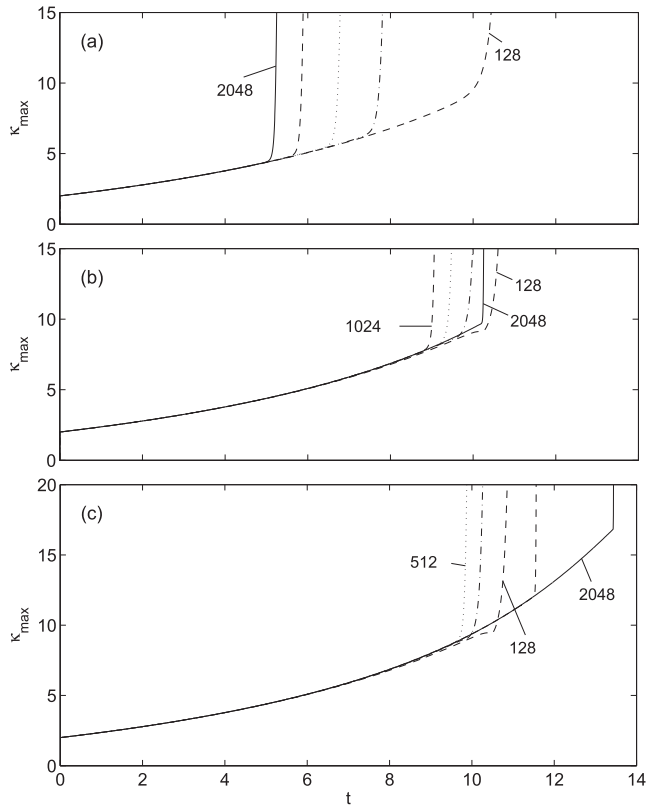

Fig. 20. Maximum curvature vs. time, computed using $N = 128$ (--), 256 (-·-), 512 (···), 1024 (--), 2048(—) and (a) the second order method, (b) the pointwise fifth order method, (c) the uniformly fifth order method. The lowest, largest and turning point values of N are labeled.

Based on these results, we expect the solution to exist for large and possibly all times, and we expect that it can be computed with sufficiently fine resolution. Furthermore, the exact solution appears to be stable to arbitrarily small perturbations. The fact that discretization error is sufficient to induce a rapid departure from it indicates that the exact solution is unstable to finite perturbations, and agrees with the observations of Rallison and Acrivos [31] and Taylor [37].

In summary, our results show that in this example: (i) Solutions to the discrete system for fixed N exist for finite time only. (ii) As N increases, the convergence is non-monotonic. N needs to be sufficiently large, $N > N_c$ until convergence in N is observed. (iii) The value N_c past which the methods converge is *smallest* for our corrected uniform fifth order method. Furthermore, for fixed $N > N_c$, the corrected method approximates the exact solution for longer times. For the second order method, on the other hand, N_c is not even reached in our simulations.

Thus, in the example presented in this section, the corrected uniform fifth order method is a significant improvement over both the second and the pointwise fifth order methods, since it converges faster and for longer times than the alternatives.

5. Summary

This paper concerns the computation of the integrals that appear in axi-symmetric interfacial Stokes flow with no swirl. We analyze a set of quadrature rules of arbitrarily large pointwise rate of convergence, based on (3.1). We use asymptotic approximations near the poles to show the existence of low order terms in the maximum quadrature error, and we construct a uniformly fifth order quadrature based on identifying the low order terms. We then apply three methods, namely the popular second order method, the pointwise fifth order method and the uniformly fifth order method, to compute the evolution of three sample flows. The examples give insight into the performance of the various methods in practice.

Our main findings are:

- Pointwise convergent methods of arbitrary high order all have a low second order term in the maximum error. Asymptotic approximations about the pole are used to identify and remove the low order terms.
- Specific formulas for a uniformly convergent fifth order method are given. With a given table of precomputed values, the method is easily implemented at no additional cost per time step.
- In the three applications presented, much is gained by using fifth order over second order accurate methods to compute the interface evolution. In particular, with equal spatial resolution, the fifth order methods
  - resolve finite time pinchoff better and to times closer to pinchoff;
  - resolve the solution near steady states better, giving significantly more accurate estimates of the steady state values;
  - simulate a continuously extending bubble accurately to longer times.
- The corrections needed to obtain uniformly fifth order errors are sometimes, but not always, significant in practice. Their significance can be deduced from their explicit representation given in Appendix D.
  - If the derivatives at the endpoints are small, the low order corrections may be much smaller than the higher order terms. In this case the corrections are not needed and the pointwise fifth order method equals the uniform fifth order method in accuracy. Examples of this scenario are the pinching bubble and low curvature steady states.
  - If derivatives at the endpoints are large, with even larger derivatives of higher order, the low order corrections may be smaller than the higher order terms, and thus not significant. In this case as well, the pointwise fifth order method equals the uniform fifth order method in accuracy. Examples of this scenario are steady states bubbles with high curvature on the axis.
  - For moderate values of endpoint curvatures and velocities the corrections improve the accuracy of the simulations. In the continuously extending bubble, this gain results in accurate solutions for longer times before instability sets in.

Acknowledgments

MN gratefully acknowledges the support of the National Science Foundation through the Grant DMS-0308061, and of the Institute for Mathematics and its Applications at the University of Minnesota during a visit in Fall 2009.

Appendix A. Functions *M* and *Q*

$$M_1^u(x,x_j,\xi) = x[I_{11} + (x^2 + x_j^2)I_{31} - xx_j(I_{30} + I_{32})], \tag{A.1a}$$
$$M_2^u(x,x_j,\xi) = x\xi(xI_{31} - x_jI_{30}), \tag{A.1b}$$
$$M_1^v(x,x_j,\xi) = x\xi(xI_{30} - x_jI_{31}), \tag{A.1c}$$
$$M_2^v(x,x_j,\xi) = x(I_{10} + \xi^2 I_{30}), \tag{A.1d}$$
$$Q_{11}^u(x,x_j,\xi) = -6x[x^3I_{51} - x^2x_j(I_{50} + 2I_{52}) + xx_j^2(I_{53} + 2I_{51}) - x_j^3I_{52}], \tag{A.1e}$$
$$Q_{12}^u(x,x_j,\xi) = -6x\xi[(x^2 + x_j^2)I_{51} - xx_j(I_{50} + I_{52})], \tag{A.1f}$$
$$Q_{21}^u(x,x_j,\xi) = Q_{12}^u, \tag{A.1g}$$
$$Q_{22}^u(x,x_j,\xi) = -6x\xi^2(xI_{51} - x_jI_{50}), \tag{A.1h}$$
$$Q_{11}^v(x,x_j,\xi) = -6x\xi(x_j^2I_{52} + x^2I_{50} - 2xx_jI_{51}), \tag{A.1i}$$
$$Q_{12}^v(x,x_j,\xi) = -6x\xi^2(xI_{50} - x_jI_{51}), \tag{A.1j}$$
$$Q_{21}^v(x,x_j,\xi) = Q_{12}^v(x,x_j,\xi), \tag{A.1k}$$
$$Q_{22}^v(x,x_j,\xi) = -6x\xi^3I_{50} \tag{A.1l}$$

with

$$I_{10} = \frac{4}{c}F(k), \tag{A.2a}$$
$$I_{11} = \frac{4}{c}a[bF(k) - E(k)], \tag{A.2b}$$

$$I_{30} = \frac{4}{c^3}E_{3/2}(k), \tag{A.2c}$$

$$I_{31} = \frac{4}{c^3}a[bE_{3/2}(k) - F(k)], \tag{A.2d}$$

$$I_{32} = \frac{4}{c^3}a^2[b^2E_{3/2}(k) - 2bF(k) + E(k)], \tag{A.2e}$$

$$I_{50} = \frac{4}{c^5}E_{5/2}(k), \tag{A.2f}$$

$$I_{51} = \frac{4}{c^5}a[bE_{5/2}(k) - E_{3/2}(k)], \tag{A.2g}$$

$$I_{52} = \frac{4}{c^5}a^2[b^2E_{5/2}(k) - 2bE_{3/2}(k) + F(k)], \tag{A.2h}$$

$$I_{53} = \frac{4}{c^5}a^3[b^3E_{5/2}(k) - 3b^2E_{3/2}(k) + 3bF(k) - E(k)], \tag{A.2i}$$

where

$$k^2 = \frac{4xx_j}{\xi^2 + (x + x_j)^2}, \tag{A.3}$$

and $a = 2/k^2,\ b = (2-k^2)/2,\ c^2 = (x+x_j)^2 + \xi^2$. Here, F and E are the complete elliptic integrals of the first and second kind, respectively:

$$F(k) = \int_0^{\pi/2} \frac{d\theta}{\sqrt{1 - k^2\sin^2\theta}}, \quad E(k) = \int_0^{\pi/2} \sqrt{1 - k^2\sin^2\theta}\, d\theta, \tag{A.4}$$

and

$$E_{3/2} = \frac{E(k)}{1-k^2}, \quad E_{5/2}(k) = \frac{2(2-k^2)}{3(1-k^2)^2}E(k) - \frac{F(k)}{3(1-k^2)}. \tag{A.5}$$

Notice that a and b are functions of k only, with $a \to 2$ and $b \to 1/2$ as $k \to 1$. Using this formulations of I_{jk} (which differs from slightly from the formulations in Lee and Leal [18]) it is easy to see that the most singular contributions to I_{3j} and I_{5j} at $k = 1$, which comes from the $E_{3/2}$ and the $E_{5/2}$ terms, respectively, are

$$I_{3j} \sim \frac{4}{c^3}\frac{1}{1-k^2}, \quad I_{5j} \sim \frac{8}{3c^5}\frac{1}{(1-k^2)^2}. \tag{A.6}$$

This fact is used in Section 3.2.

Appendix B. Integrands for $\alpha_j = 0, \pi$

The limits of the integrands in (2.10a) and (2.10b) as $\alpha_j \to 0, \pi$ are found by expanding M and Q about $x_j = 0$ using known expansions of $F(k)$ and $E(k)$ about $k = 0$ to be

$$G_s^u(\alpha, \alpha_{jend}, t) = 0, \tag{B.1}$$

$$G_s^v(\alpha, \alpha_{jend}, t) = \frac{2\pi x\kappa}{(x^2+\xi^2)^{3/2}}[\dot{y}x\xi - \dot{x}(2\xi^2 + x^2)], \tag{B.2}$$

$$G_d^u(\alpha, \alpha_{jend}, t) = 0, \tag{B.3}$$

$$G_d^v(\alpha, \alpha_{jend}, t) = -\frac{12\pi x\xi}{(x^2+\xi^2)^{5/2}}(ux + v\xi)(x\dot{y} - \xi\dot{x}), \tag{B.4}$$

where $jend = 0$ or n, and $x = x(\alpha),\ y = y(\alpha),\ \xi = y(\alpha) - y_{jend}$. The values and derivatives of G_s^v at the endpoints, needed to implement the quadrature rule (3.5), are:

$$G_s^v(0,0,t) = -2\pi\kappa_0|\dot{x}_0|, \quad \frac{d}{d\alpha}G_s^v(0,0,t) = 0, \quad \frac{d^3}{d\alpha^3}G_s^v(0,0,t) = 0, \quad G_s^v(\pi,0,t) = 0, \quad \frac{d}{d\alpha}G_s^v(\pi,0,t) = -\frac{4\pi\kappa_n\dot{x}_n^2}{|\xi|},$$
$$\frac{d^3}{d\alpha^3}G_s^v(\pi,0,t) = -\frac{4\pi\dot{x}_n}{|\xi|^3}[3\ddot{\kappa}_n\dot{x}_n\xi^2 - \kappa_n(6\dot{x}_n^3 - 4\ddot{x}_n\xi^2 + 6\dot{x}_n\xi\ddot{y}_n)], \tag{B.5}$$

$$G_s^v(\pi,\pi,t) = 2\pi\kappa_n|\dot{x}_n|, \quad \frac{d}{d\alpha}G_s^v(\pi,\pi,t) = 0, \quad \frac{d^3}{d^3\alpha}G_s^v(\pi,\pi,t) = 0, \quad G_s^v(0,\pi,t) = 0, \quad \frac{d}{d\alpha}G_s^v(0,\pi,t) = -\frac{4\pi\kappa_0\dot{x}_0^2}{|\xi|},$$
$$\frac{d^3}{d\alpha^3}G_s^v(0,\pi,t) = \frac{4\pi\dot{x}_0}{|\xi|^3}[-3\ddot{\kappa}_0\dot{x}_0\xi^2 + \kappa_0(6\dot{x}_0^3 - 4\ddot{x}_0\xi^2 - 6\dot{x}_0\xi\ddot{y}_0)], \tag{B.6}$$

where $\xi = y_n - y_0$. Similarly, the values for G_d^v are:

$$G_d^v(0,0,t) = 0, \quad \frac{d}{d\alpha}G_d^v(0,0,t) = 0, \quad \frac{d^3}{d\alpha^3}G_d^v(0,0,t) = 0, \quad G_d^v(\pi,0,t) = 0, \quad \frac{d}{d\alpha}G_d^v(\pi,0,t) = \frac{12\pi v_n \dot{x}_n^2}{\xi|\xi|},$$
$$\frac{d^3}{d\alpha^3}G_d^v(\pi,0,t) = \frac{12\pi\dot{x}_n}{\xi^3|\xi|}[3\dot{x}_n\xi(2\dot{u}_n\dot{x}_n + \ddot{v}_n\xi) - v_n(15\dot{x}_n^3 - 4\ddot{x}_n\xi^2 + 12\dot{x}_n\xi\ddot{y}_n)], \tag{B.7}$$

$$G_d^v(\pi,\pi,t) = 0, \quad \frac{d}{d\alpha}G_d^v(\pi,\pi,t) = 0, \quad \frac{d^3}{d^3\alpha}G_d^v(\pi,\pi,t) = 0, \quad G_d^v(0,\pi,t) = 0, \quad \frac{d}{d\alpha}G_d^v(0,\pi,t) = -\frac{12\pi v_0 \xi \dot{x}_0^2}{|\xi|^3},$$
$$\frac{d^3}{d\alpha^3}G_d^v(0,\pi,t) = \frac{12\pi\dot{x}_0}{\xi^3|\xi|}[3\dot{x}_0\xi(2\dot{u}_0\dot{x}_0 - \ddot{v}_0\xi) + v_0(15\dot{x}_0^3 - 4\ddot{x}_0\xi^2 - 12\dot{x}_0\xi\ddot{y}_0)], \tag{B.8}$$

where, as above, $\xi = y_n - y_0$.

Appendix C. Relevant coefficients of $G(\alpha, \alpha_j, t)$

This appendix lists all the coefficients c_k of G and its derivatives at the endpoints needed to implement the pointwise fifth order quadrature T_5, given in (3.5). For $G^{u,s}(\alpha, \alpha_j, t)$, $\alpha_j \neq 0, \pi$, the values are:

$$\widetilde{G}^{u,s}(\alpha_j, \alpha_j, 0) = 0, \tag{C.1}$$
$$c_2^{u,s} = -\ddot{\kappa}_j\dot{y}_j - \frac{2\dot{\kappa}_j}{x_j}(\dot{x}_j\dot{y}_j + \ddot{y}_j x_j), \tag{C.2}$$

$$\frac{dG^{u,s}}{d\alpha}(0,\alpha_j,t) = \frac{2\pi(\kappa_0 - \kappa_j)\dot{x}_0^2 x_j \xi}{[x_j^2 + \xi^2]^{3/2}}, \quad \xi = y_0 - y_j, \tag{C.3a}$$
$$\frac{dG^{u,s}}{d\alpha}(\pi,\alpha_j,t) = \frac{2\pi(\kappa_n - \kappa_j)\dot{x}_n^2 x_j \xi}{[x_j^2 + \xi^2]^{3/2}}, \quad \xi = y_n - y_j, \tag{C.3b}$$

$$\frac{d^3G^{u,s}}{d\alpha^3}(0,\alpha_j,t) = \frac{\pi\dot{x}_0 x_j}{[x_j^2 + \xi^2]^{7/2}}[(\kappa_0 - \kappa_j)[12\dot{x}_0\ddot{y}_0(x_j^4 - x_j^2\xi^2 - 2\xi^4) + 9\dot{x}_0^3(x_j^2 - 4\xi^2)\xi + 8\ddot{x}_0(x_j^2 + \xi^2)^2\xi]$$
$$+ 6\ddot{\kappa}_0\dot{x}_0(x_j^2 + \xi^2)^2\xi], \quad \xi = y_0 - y_j, \tag{C.4a}$$

$$\frac{d^3G^{u,s}}{d\alpha^3}(\pi,\alpha_j,t) = \frac{\pi\dot{x}_n x_j}{[x_j^2 + \xi^2]^{7/2}}[(\kappa_n - \kappa_j)[12\dot{x}_n\ddot{y}_n(x_j^4 - x_j^2\xi^2 - 2\xi^4) + 9\dot{x}_n^3(x_j^2 - 4\xi^2)\xi + 8\ddot{x}_n(x_j^2 + \xi^2)^2\xi]$$
$$+ 6\ddot{\kappa}_n\dot{x}_n(x_j^2 + \xi^2)^2\xi], \quad \xi = y_n - y_j. \tag{C.4b}$$

For $G^{v,s}$, $\alpha_j \neq 0, \pi$, the values are:

$$\widetilde{G}^{v,s}(\alpha_j, \alpha_j, 0) = 0, \tag{C.5}$$
$$c_2^{v,s} = \ddot{\kappa}_j\dot{x}_j + \frac{\dot{\kappa}_j}{x_j}(\dot{x}_j^2 + 2x_j\ddot{x}_j - \dot{y}_j^2), \tag{C.6}$$

$$\frac{dG^{v,s}}{d\alpha}(0,\alpha_j,t) = -\frac{2\pi(\kappa_0 - \kappa_j)\dot{x}_0^2(x_j^2 + 2\xi^2)}{[x_j^2 + \xi^2]^{3/2}}, \quad \xi = y_0 - y_j, \tag{C.7a}$$
$$\frac{dG^{v,s}}{d\alpha}(\pi,\alpha_j,t) = -\frac{2\pi(\kappa_n - \kappa_j)\dot{x}_n^2(x_j^2 + 2\xi^2)}{[x_j^2 + \xi^2]^{3/2}}, \quad \xi = y_n - y_j, \tag{C.7b}$$

$$\frac{d^3G^{v,s}}{d\alpha^3}(0,\alpha_j,t) = \frac{\pi\dot{x}_0}{[x_j^2 + \xi^2]^{7/2}}[(\kappa_0 - \kappa_j)[-8\ddot{x}_0(x_j^2 + \xi^2)^2(x_j^2 + 2\xi^2) - 3\dot{x}_0^3(x_j^4 + 8x_j^2\xi^2 - 8\xi^4) + 12\dot{x}_0\ddot{y}_0(-x_j^4 + x_j^2\xi^2$$
$$+ 2\xi^4)\xi] - 6\ddot{\kappa}_0\dot{x}_0(x_j^2 + \xi^2)^2(x_j^2 + 2\xi^2)], \quad \xi = y_0 - y_j, \tag{C.8a}$$

$$\frac{d^3G^{v,s}}{d\alpha^3}(\pi,\alpha_j,t) = \frac{\pi\dot{x}_n}{[x_j^2 + \xi^2]^{7/2}}[(\kappa_n - \kappa_j)[-8\ddot{x}_n(x_j^2 + \xi^2)^2(x_j^2 + 2\xi^2) - 3\dot{x}_n^3(x_j^4 + 8x_j^2\xi^2 - 8\xi^4) + 12\dot{x}_n\ddot{y}_n(-x_j^4 + x_j^2\xi^2$$
$$+ 2\xi^4)\xi] - 6\ddot{\kappa}_n\dot{x}_n(x_j^2 + \xi^2)^2(x_j^2 + 2\xi^2)], \quad \xi = y_n - y_j.$$

For $G^{u,d}$, $\alpha_j \neq 0, \pi$, the values are:

$$\widetilde{G}^{u,d}(\alpha_j,\alpha_j,0) = \frac{-2v_j\dot{x}_j\dot{y}_j(\dot{y}_j(\dot{x}_j^2+\dot{y}_j^2)-2x_j(\ddot{x}_j\dot{y}_j-\dot{x}_j\ddot{y}_j))}{x_j(\dot{x}_j^2+\dot{y}_j^2)^2} + \frac{2u_j(\dot{y}_j(2\dot{x}_j^4+3\dot{y}_j^4)+\dot{x}_j^2\dot{y}_j(2x_j\ddot{x}_j+5\dot{y}_j^2)-2x_j\dot{x}_j^3\ddot{y}_j)}{x_j(\dot{x}_j^2+\dot{y}_j^2)^2} \tag{C.9}$$

$$c_2^{u,d} = \frac{3}{4x_j^3}(\dot{y}_j(-4\dot{v}_j x_j\dot{y}_j+3v_j\dot{x}_j\dot{y}_j-6v_j x_j\ddot{y}_j)+u_j(2\dot{x}_j^2\dot{y}_j+2x_j\ddot{x}_j\dot{y}_j+5\ddot{y}_j^3-2x_j\dot{x}_j\ddot{y}_j)) \tag{C.10}$$

$$\frac{dG^{u,d}}{d\alpha}(0,\alpha_j,t) = \frac{-12\pi v_0\dot{x}_0^2\xi^2 x_j}{(x_j^2+\xi^2)^{5/2}}, \quad \xi = y_j - y_0, \tag{C.11a}$$

$$\frac{dG^{u,d}}{d\alpha}(\pi,\alpha_j,t) = \frac{-12\pi v_n\dot{x}_n^2\xi^2 x_j}{(x_j^2+\xi^2)^{5/2}}, \quad \xi = y_j - y_n, \tag{C.11b}$$

$$\frac{d^3G^{u,d}}{d\alpha^3}(0,\alpha_j,t) = \frac{6\pi x_j\dot{x}_0}{(x_j^2+\xi^2)^5}\left[2(3x_j^2\dot{u}_0\ddot{y}_0-\xi^2(3\dot{x}_0\dddot{v}_0+4\ddot{x}_0v_0))+\frac{6\dot{x}_0\xi(2x_j^2-3\xi^2)}{x_j^2+\xi^2}(\dot{x}_0\dot{u}_0-2v_0\ddot{y}_0)+\frac{15\dot{x}_0^3\xi^2v_0}{(x_j^2+\xi^2)^2}(-3x_j^2+4\xi^2)\right], \quad \xi = y_0 - y_j, \tag{C.12a}$$

$$\frac{d^3G^{u,d}}{d\alpha^3}(\pi,\alpha_j,t) = \frac{6\pi x_j\dot{x}_n}{(x_j^2+\xi^2)^5}\left[2(3x_j^2\dot{u}_n\ddot{y}_n-\xi^2(3\dot{x}_n\dddot{v}_n+4\ddot{x}_nv_n))+\frac{6\dot{x}_n\xi(2x_j^2-3\xi^2)}{x_j^2+\xi^2}(\dot{x}_n\dot{u}_n-2v_n\ddot{y}_n)+\frac{15\dot{x}_n^3\xi^2v_n}{(x_j^2+\xi^2)^2}(-3x_j^2+4\xi^2)\right], \quad \xi = y_n - y_j. \tag{C.12b}$$

For $G^{v,d}$, $\alpha_j \neq 0, \pi$, the values are:

$$\widetilde{G}^{v,d}(\alpha_j,\alpha_j,0) = \frac{-2\dot{y}_j(u_j\dot{x}_j+v_j\dot{y}_j)(\dot{x}_j^2\dot{y}_j-2x_j\ddot{x}_j\dot{y}_j+\dot{y}_j^3+2x_j\dot{x}_j\ddot{y}_j)}{x_j(\dot{x}_j^2+\dot{y}_j^2)^2}, \tag{C.13}$$

$$c_2^{v,d} = \frac{3\dot{y}_j}{4x_j^3}(4\dot{u}_j x_j\dot{y}_j-5u_j\dot{x}_j\dot{y}_j+v_j\dot{y}_j^2+6u_j x_j\ddot{y}_j), \tag{C.14}$$

$$\frac{dG^{v,d}}{d\alpha}(0,\alpha_j,t) = \frac{12\pi v_0\dot{x}_0^2\xi^3}{(x_j^2+\xi^2)^{5/2}}, \quad \xi = y_j - y_0, \tag{C.15a}$$

$$\frac{dG^{v,d}}{d\alpha}(\pi,\alpha_j,t) = \frac{12\pi v_n\dot{x}_n^2\xi^3}{(x_j^2+\xi^2)^{5/2}}, \quad \xi = y_j - y_n, \tag{C.15b}$$

$$\frac{d^3G^{v,d}}{d\alpha^3}(0,\alpha_j,t) = \frac{6\pi\xi\dot{x}_0}{(x_j^2+\xi^2)^5}\left[2(-3x_j^2\dot{u}_0\ddot{y}_0+\xi^2(3\dot{x}_0\dddot{v}_0+4\ddot{x}_0v_0))+\frac{6\dot{x}_0\xi(3x_j^2-2\xi^2)}{x_j^2+\xi^2}(-\dot{x}_0\dot{u}_0+2v_0\ddot{y}_0)+\frac{15\dot{x}_0^3\xi^2v_0}{(x_j^2+\xi^2)^2}(5x_j^2-2\xi^2)\right], \quad \xi = y_0 - y_j, \tag{C.16a}$$

$$\frac{d^3G^{v,d}}{d\alpha^3}(\pi,\alpha_j,t) = \frac{6\pi\xi\dot{x}_n}{(x_j^2+\xi^2)^5}\left[2(-3x_j^2\dot{u}_n\ddot{y}_n+\xi^2(3\dot{x}_n\dddot{v}_n+4\ddot{x}_nv_n))+\frac{6\dot{x}_n\xi(3x_j^2-2\xi^2)}{x_j^2+\xi^2}(-\dot{x}_n\dot{u}_n+2v_n\ddot{y}_n)+\frac{15\dot{x}_n^3\xi^2v_n}{(x_j^2+\xi^2)^2}(5x_j^2-2\xi^2)\right], \quad \xi = y_n - y_j. \tag{C.16b}$$

For $\alpha_j = 0, \pi$ the function $G_s^u(\alpha,\alpha_j,t) = 0$. The function $G_s^v(\alpha,\alpha_j,t)$ given by (2.8b) is smooth, so $c_0 = c_2 = 0$ and $\widetilde{G}_s^v(\alpha_j,\alpha_j,t) = G_s^v(\alpha_j,\alpha_j,t)$. For $\alpha_j = 0$, the derivatives at the endpoints are given in Appendix B.

Appendix D. Approximating functions $B(\alpha,\alpha_j,t)$

This appendix lists the functions $b^l(t)$ and $B(\eta)$ in the approximation (3.20) and (3.21) of G near the left pole. Throughout it, $\eta = \alpha/\alpha_j$ and $k^2 = 4\eta/(1+\eta)^2$. The functions $b^r(t)$ are obtained from the formulas for $b^l(t)$ by replacing the subscript 0 by n

$$b_1^{l,us}(t) = \frac{\ddot{\kappa}_0 \dot{x}_0 \ddot{y}_0}{|\dot{x}_0|}, \quad B_1^{us}(\eta) = \frac{\eta}{2}(1-\eta^2)\left[3(1+\eta)E(k) - \left(\frac{1+3\eta^2}{1+\eta}\right)F(k)\right], \tag{D.1}$$

$$b_1^{l,vs}(t) = \frac{\ddot{\kappa}_0 \dot{x}_0^2}{|\dot{x}_0|}, \quad B_1^{vs}(\eta) = -2\eta\frac{\eta^2-1}{1+\eta}F(k), \tag{D.2}$$

$$b_1^{l,ud}(t) = \frac{v_0 \ddot{y}_0^2}{\dot{x}_0|\dot{x}_0|}, \quad B_1^{ud}(\eta) = -3\eta[(1+\eta)E(k) + (1-\eta)F(k)], \tag{D.3}$$

$$b_2^{l,ud}(t) = \frac{\dot{u}_0}{\dot{x}_0|\dot{x}_0|}\left[\frac{4}{3}\dddot{x}_0\ddot{y}_0 + \frac{5}{2}\frac{\ddot{y}_0^3}{\dot{x}_0} - \frac{1}{3}\dddot{y}_0\dot{x}_0\right], \quad B_2^{ud}(\eta) = \eta(1+\eta)\left[(1+\eta^2)E(k) - (1-\eta)^2F(k)\right], \tag{D.4}$$

$$b_3^{l,ud}(t) = \frac{v_0\dddot{x}_0\ddot{y}_0^2}{\dot{x}_0^2|\dot{x}_0|}, \quad B_3^{ud}(\eta) = \frac{\eta}{6}\left[(1+\eta)(23+5\eta^2)E(k) + (1-\eta)(1+5\eta^2)F(k)\right], \tag{D.5}$$

$$b_4^{l,ud}(t) = \frac{v_0\ddot{y}_0\dddot{y}_0}{\dot{x}_0|\dot{x}_0|}, \quad B_4^{ud}(\eta) = -\frac{\eta}{6}\left[5(1+\eta+\eta^2+\eta^3)E(k) + (1-\eta)(1+5\eta^2)F(k)\right], \tag{D.6}$$

$$b_5^{l,ud}(t) = \frac{\ddot{v}_0\ddot{y}_0^2}{\dot{x}_0|\dot{x}_0|}, \quad B_5^{ud}(\eta) = -\frac{3\eta^3}{2}[(1+\eta)E(k) + (1-\eta)F(k)], \tag{D.7}$$

$$b_6^{l,ud}(t) = \frac{v_0\ddot{y}_0^4}{\dot{x}_0^3|\dot{x}_0|}, \quad B_6^{ud}(\eta) = \frac{5}{8}\eta(1+\eta)\left[(7+\eta^2)E(k) - (1-\eta)^2F(k)\right]. \tag{D.8}$$

$$b_1^{vd}(t) = \frac{\dot{u}_0\ddot{y}_0^2}{\dot{x}_0|\dot{x}_0|}, \quad B_1^{vd}(\eta) = -3\eta[(1+\eta)E(k) + (\eta-1)F(k)], \tag{D.9}$$

$$b_2^{vd}(t) = \frac{v_0\ddot{y}_0^3}{\dot{x}_0^2|\dot{x}_0|}, \quad B_2^{vd}(\eta) = -3\eta(1+\eta)E(k). \tag{D.10}$$

Appendix E. Relevant coefficients of B_s^u

The functions $B_k^{u/v,s/d}$ are all of the form

$$B_k(\eta) = \widetilde{B}_k(\eta) + \sum_{l=1}^{\infty} c_{kj}(\eta-1)^j \log|\eta-1|. \tag{E.1}$$

Here, we list the coefficients and derivatives necessary to compute $E_5[B]$, using (3.5), for the single layer only, as examples. The results are obtained with Mathematica. All real numbers are rounded to as many digits as listed.

$$c_{1,2}^{u,s} = -5, \quad \widetilde{B}_1^{u,s}(1) = 0, \quad \frac{dB_1^{u,s}}{d\eta}(0) = \pi/2, \quad \frac{d^3B_1^{u,s}}{d\eta^3}(0) = -27\pi/4, \tag{E.2}$$

$$\frac{dB_1^{u,s}}{d\eta}(10) = 15.70828565, \quad \frac{d^3B_1^{u,s}}{d^3\eta}(10) = 0.00003929, \tag{E.3}$$

$$c_{1,2}^{v,s} = 2, \quad \widetilde{B}_1^{v,s}(1) = 0, \quad \frac{dB_1^{v,s}}{d\eta}(0) = \pi, \quad \frac{d^3B_1^{v,s}}{d\eta^3}(0) = -9\pi/2, \tag{E.4}$$

$$\frac{dB_1^{v,s}}{d\eta^3}(10) = -62.8325457383, \quad \frac{d^3B_1^{v,s}}{d\eta^3}(10) = -0.0000841112. \tag{E.5}$$

References

[1] A. Acrivos, The breakup of small drops and bubbles in shear flows, Ann. N.Y. Acad. Sci. 404 (1983) 1–11.
[2] R. Almgren, Singularity formation in Hele–Shaw bubbles, Phys. Fluids 8 (2) (1996) 344–352.
[3] G.R. Baker, D.I. Meiron, S.A. Orszag, Boundary integral methods for axisymmetric and three dimensional Rayleigh–Taylor instability problems, Physica D 12 (1984) 19–31.
[4] I.B. Bazhlekov, P.D. Anderson, H.E.H. Meijer, Boundary integral method for deformable interfaces in the presence of insoluble surfactants, Lect. Notes Comput. Sci. 2907 (2004) 355–362.
[5] I.B. Bazhlekov, P.D. Anderson, H.E.H. Meijer, Nonsingular boundary integral method for deformable drops in viscous flows, Phys. Fluids 16 (2004) 1064–1081.
[6] J. Blawzdziewicz, Boundary integral methods for stokes flow, in: A. Prosperetti, G. Tryggvason (Eds.), Computational Methods for Multiphase Flows, Cambridge University Press, 2007, pp. 193–236.
[7] J.P. Boyd, The erfc-log filter and the asymptotics of the Euler and Vandeven sequence accelerations, in: A.V. Ilin, L.R. Scott (Eds.), Proceedings of the Third International Conference on Spectral and High Order Methods, Houston J. Math. (1996) 267–276.
[8] R. Bulirsch, Numerical calculation of elliptic integrals and elliptic functions, Numer. Math. 7 (1965) 78–90.
[9] H.D. Ceniceros, H. Si, Computation of axisymmetric suction flow through porous media in the presence of surface tension, J. Comput. Phys. 165 (2000) 237–260.
[10] V. Cristini, J. Blawzdziewich, M. Loewenberg, Drop breakup in three-dimensional viscous flows, Phys. Fluids 10 (1998) 1781–1783.
[11] R.H. Davis, Buoyancy-driven viscous interaction of a rising drop with a smaller trailing drop, Phys. Fluids 11 (5) (1999) 1016–1028.

[12] B. de Bernadinis, D.W. Moore, A ring-vortex representation of an axi-symmetric vortex sheet, in: Studies of Vortex Dominated Flows, Springer, 1987, pp. 33–43.
[13] J. Eggers, S.C. du Pont, Numerical analysis of tips in viscous flow, Phys. Rev. E 79 (6) (2009) 066311(16).
[14] C.D. Eggleton, Y.P. Pawar, K.J. Stebe, Insoluble surfactants on a drop in an extensional flow: a generalization of the stagnated surface limit to deforming interfaces, J. Fluid Mech. 385 (1999) 79–99.
[15] C.D. Eggleton, T.-M. Tsai, K.J. Stebe, Tip streaming from a drop in the presence of surfactants, Phys. Rev. Lett. 87 (4) (2001) 048302-1–048302-4.
[16] V. Frayssé, L. Giraud, S. Gratton, J. Langou, A set of GMRES routines for real and complex arithmetics on high performance computers. Tech. Rep. TR/PA/03/3, CERFACS, 2003.
[17] T.Y. Hou, J.S. Lowengrub, M.J. Shelley, Removing the stiffness from interfacial flows with surface tension, J. Comput. Phys. 114 (1994) 312–338.
[18] S.H. Lee, L.G. Leal, The motion of a sphere in the presence of a deformable interface. II. A numerical study of a translation of a sphere normal to an interface, J. Colloid Interface 87 (1982) 81–106.
[19] J.R. Lister, A.B. Thompson, A. Perriot, L. Duchemin, Shape and stability of axisymmetric levitated viscous drops, J. Fluid Mech. 617 (2008) 167–185.
[20] M. Manga, H. Stone, Buoyancy-driven interactions between deformable drops at low reynolds numbers, J. Fluid Mech. 256 (1993) 647–683.
[21] M. Nemer, X. Chen, D. Papadopoulos, J. Blawzdziewicz, M. Loewenberg, Hindered and enhanced coalescence of drops in stokes flow, Phys. Rev. Lett. 92 (2004) 114501-1–114501-4.
[22] Q. Nie, G. Baker, Application of adaptive quadrature to axi-symmetric vortex sheet motion, J. Comput. Phys. 143 (1998) 49–69.
[23] M. Nitsche, Axisymmetric vortex sheet motion: accurate evaluation of the principal value integral, SIAM J. Sci. Comput. 21 (3) (1999) 1066–1084.
[24] M. Nitsche, Singularity formation in a cylindrical and a spherical vortex sheet, J. Comput. Phys. 173 (1) (2001) 208–230.
[25] M. Nitsche, P.H. Steen, Numerical simulations of inviscid capillary pinchoff, J. Comput. Phys. 200 (2004) 299–324.
[26] C. Pozrikidis, Boundary Integral and Singularity Methods for Linearized Viscous Flow, Cambridge University Press, Cambridge, UK, 1992.
[27] C. Pozrikidis, Numerical studies of cusp formation at fluid interfaces in stokes flow, J. Fluid. Mech. 357 (1998) 29–57.
[28] C. Pozrikidis, Interfacial dynamics for Stokes flows, J. Comput. Phys. 169 (2) (2001) 250–301.
[29] D.A. Pugh, Development of Vortex Sheets in Boussinesq Flows – Formation of Singularities. Ph.D. Thesis, Imperial College of Science and Technology, 1989.
[30] J.M. Rallison, The deformation of small viscous drops and bubbles in shear flows, Annu. Rev. Fluid Mech. 16 (1984) 45–66.
[31] J.M. Rallison, A. Acrivos, A numerical study of the deformation and burst of a viscous drop in an extensional flow, J. Fluid Mech. 89 (1978) 191–200.
[32] A. Sidi, M. Israeli, Quadrature methods for periodic singular and weakly singular Fredholm integral equations, J. Sci. Comput. 3 (2) (1988) 201–231.
[33] M. Siegel, Cusp formation for time-evolving bubbles in two-dimensional stokes flow, J. Fluid Mech. 412 (2000) 227–257.
[34] A. Sierou, J.R. Lister, Self-similar solutions for viscous capillary pinch-off, J. Fluid Mech. 497 (2003) 381–403.
[35] H.A. Stone, Dynamics of drop deformation and breakup in viscous fluids, Annu. Rev. Fluid Mech. 26 (1994) 65–102.
[36] H.A. Stone, L.G. Leal, Relaxation and breakup of an initially extended drop in an otherwise quiescent fluid, J. Fluid Mech. 198 (1989) 399–427.
[37] G.I. Taylor, The formation of emulsions in definable fields of flow, Proc. Roy. Soc. London A 146 (1934) 501–523.
[38] C.F. Van Loan, Introduction to Scientific Computing, Prentice-Hall, Upper Saddle River, NJ, 2000.
[39] Y. Yoon, F. Baldessari, H.D. Ceniceros, L.G. Leal, Coalescence of two equally-sized deformable drops in an axisymmetric flow, Phys. Fluids 19 (10) (2007).
[40] G.K. Youngren, A. Acrivos, On the shape of a gas bubble in a viscous extensional flow, J. Fluid Mech. 76 (1976) 433.
[41] Z. Zapryanov, S. Tabakova, Dynamics of Bubbles, Drops and Rigid Particles, Fluid Mechanics and its Applications, vol. 50, Kluwer Academic Publishers., Dordrecht, Boston, Mass, 1999.
[42] A.Z. Zinchenko, M.A. Rother, R.H. Davis, A novel boundary integral algorithm for viscous interaction of deformable drops, Phys. Fluids 9 (1997) 1493–1511.